The Astrophysical Journal, 953:170 (23pp), 2023 August 20 https://doi.org/10.3847/1538-4357/ace32e

Brown Dwarf Retrievals on FIRE!: Atmospheric Constraints and Lessons Learned from High Signal-to-noise Medium-resolution Spectroscopy of a T9 Dwarf

Callie E. Hood[1], Jonathan J. Fortney[1], Michael R. Line[2], and Jacqueline K. Faherty[3]
[1] Department of Astronomy & Astrophysics, University of California, Santa Cruz, CA 95064, USA; cehood@ucsc.edu
[2] School of Earth and Space Exploration, Arizona State University, Tempe, AZ 85287, USA
[3] Department of Astrophysics, American Museum of Natural History, Central Park West at 79th Street, NY 10024, USA

Received 2023 March 7; revised 2023 June 25; accepted 2023 June 27; published 2023 August 16

Abstract

Brown dwarf spectra offer vital testbeds for our understanding of the chemical and physical processes that sculpt substellar atmospheres. Recently, atmospheric retrieval approaches have been successfully applied to low-resolution ($R \sim 100$) spectra of L, T, and Y dwarfs, yielding constraints on the chemical abundances and temperature structures of these atmospheres. Medium-resolution ($R \sim 10^3$) spectra of brown dwarfs offer additional insight, as molecular features are more easily disentangled and the thermal structure of the upper atmosphere is better probed. We present results from a GPU-based retrieval analysis of a high signal-to-noise, medium-resolution ($R \sim 6000$) FIRE spectrum from 0.85 to 2.5 μm of the T9 dwarf UGPS J072227.51–054031.2. At 60× higher spectral resolution than previous brown dwarf retrievals, a number of novel challenges arise. We examine the effect of different opacity sources, in particular for CH_4. Furthermore, we find that flaws in the data like errors from order stitching can bias our constraints. We compare these retrieval results to those for an $R \sim 100$ spectrum of the same object, revealing how constraints on atmospheric abundances and temperatures improve by an order of magnitude or more with increased spectral resolution. In particular, we can constrain the abundance of H_2S, which is undetectable at lower spectral resolution. While these medium-resolution retrievals offer the potential of precise, stellar-like constraints on atmospheric abundances (∼0.02 dex), our retrieved radius is unphysically small ($R = 0.50^{+0.01}_{-0.01}\,R_{\rm Jup}$), indicating shortcomings with our modeling framework. This work is an initial investigation into brown dwarf retrievals at medium spectral resolution, offering guidance for future ground-based studies and JWST observations.

Unified Astronomy Thesaurus concepts: Brown dwarfs (185); T dwarfs (1679); Atmospheric composition (2120); Bayesian statistics (1900)

Supporting material: data behind figure

1. Introduction

Brown dwarfs, objects more massive than gas giant planets but yet not massive enough to sustain hydrogen fusion like a star (13 $M_{\rm Jup} \lesssim {\rm M} \lesssim 73\,M_{\rm Jup}$; Burrows et al. 2001), provide essential testbeds of our understanding of the physics and chemical processes that sculpt substellar atmospheres. Without a sustained central energy source from fusion, brown dwarfs instead cool over time, leading to the formation of molecules and condensates in their atmospheres which dramatically affect their emitted spectra across the M, L, T, and Y spectral types (e.g., Kirkpatrick 2005; Cushing et al. 2011). The chemical and physical processes shaping these spectra are expected to be similar to those of gas giant exoplanets due to their similar effective temperatures (Faherty et al. 2016). Thus, the often more easily observable spectra of brown dwarfs can inform our predictions for and interpretations of spectra of directly imaged planets.

Traditionally, brown dwarf spectra have been compared to theoretical "grid models" which use our current understanding of substellar atmospheres and evolution to produce model spectra for a small number of fundamental parameters, such as composition, effective temperature, and surface gravity (see Marley & Robinson 2015 for a review). The cost of a small number of parameters is the number of chemical and physical assumptions, for example radiative-convective and thermochemical equilibrium, that are required. These grid models are an important resource for connecting observed properties with the physical parameters of brown dwarfs as well as predicting signatures to be tested with future observations. However, while advancements in molecular opacities and increasing model complexity have led to improved fits to observed spectra (Phillips et al. 2020; Marley et al. 2021), notable discrepancies remain (Leggett et al. 2021), indicating there is still much to be learned about modeling these cool atmospheres.

An alternative way to glean information from brown dwarf spectra is atmospheric retrieval, a data-driven Bayesian inverse method where minimal assumptions are made at the cost of far more free parameters. First developed for Earth and solar system sciences (e.g., Rodgers 2000; Fletcher et al. 2007) and then adapted for exoplanets (e.g., Madhusudhan & Seager 2009; Benneke & Seager 2012; Line et al. 2013), atmospheric retrievals have been applied successfully to brown dwarf spectra of various spectral types (Line et al. 2014, 2015; Burningham et al. 2017; Line et al. 2017; Zalesky et al. 2019; Gonzales et al. 2020; Kitzmann et al. 2020; Piette & Madhusudhan 2020; Burningham et al. 2021; Gonzales et al. 2021; Calamari et al. 2022; Gonzales et al. 2022; Howe et al. 2022; Lueber et al. 2022; Wang et al. 2022; Xuan et al. 2022; Zalesky et al. 2022). Retrievals provide a way to test the assumptions included in grid models; for example, Line et al. (2017) and Zalesky et al. (2019) used retrievals of T and Y dwarfs to show a decrease of Na and K abundances with

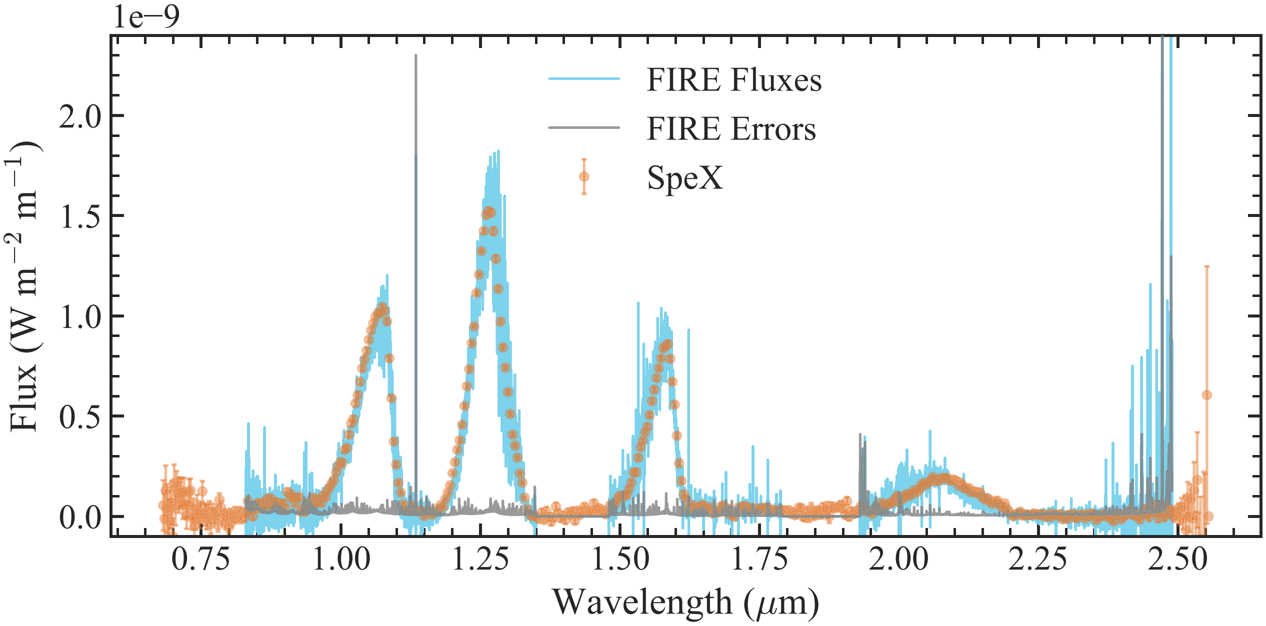

Figure 1. The FIRE (B11; $R \sim 6000$) and SpeX (Burgasser 2014; $R \sim 87$–300) spectra of UGPS 0722. The FIRE fluxes are in blue, FIRE errors in gray, and SpeX data points in orange. The FIRE spectrum is available for download online as supplementary data.

(The data used to create this figure are available.)

effective temperature, validating the rainout chemistry paradigm over pure equilibrium. However, while atmospheric retrieval can explore a wider range of possible atmospheres, unphysical combinations of parameters can still provide good fits to the data and therefore spuriously be preferred in retrieval frameworks. In particular, a number of brown dwarf retrieval studies have yielded unphysically small radius constraints (e.g., Burningham et al. 2021; Lueber et al. 2022) or very high surface gravities (Zalesky et al. 2019). Therefore, comparison to theoretical expectations from grid models are still needed to ensure retrieval results are fully contextualized.

A vast majority of brown dwarf retrieval studies have been conducted on low-resolution ($R \sim 100$) spectra. At medium-resolution, $R \gtrsim 1000$, molecular bandheads are resolved into unique groups of densely packed lines, allowing for more robust detections of molecules. Furthermore, the cores of strong lines are formed at lower pressures than can be sensed at low spectral resolutions, providing better probes of the upper end of the atmosphere's temperature–pressure (TP) profile. Comparisons of medium-resolution spectra of brown dwarfs to grid models have provided validations of certain line lists (Canty et al. 2015) and constraints on the brown dwarf's fundamental properties (e.g., Bochanski et al. 2011; Hoch et al. 2022; Petrus et al. 2023). Spectroscopy at medium-to-high spectral resolutions of brown dwarfs have been analyzed in retrieval frameworks, but often over a narrow wavelength range and with relatively low signal-to-noise, though they can also be combined with low-resolution observations for better constraints (Wang et al. 2022; Xuan et al. 2022).

The aim of this work is to test how the atmospheric retrieval framework works at medium spectral resolution ($R \sim 6000$), in terms of both new insights and novel challenges. We use the same framework successfully applied at low resolution (e.g., Line et al. 2017; Zalesky et al. 2022) for a spectrum with roughly 60× higher spectral resolution. This work is structured as follows. In Section 2, we describe our data set, retrieval framework, and the modifications necessary at this spectral resolution. In Section 3, we give an overview of the tests performed and changes made throughout this project, and the accompanying results and lessons learned. In Section 4, we put our results in context with constraints from low-resolution spectra of the same object, including a previous analysis of this data set, and grid models. Finally, our conclusions are summarized in Section 5.

2. Methods

2.1. Spectra of UGPS 0722

We perform our analysis on the medium-resolution spectrum of UGPS 0722 presented by Bochanski et al. (2011; hereafter B11) obtained with the Folded-port InfraRed Echellette (FIRE; Simcoe et al. 2013) at the Magellan Telescopes. This spectrum covers 0.85–2.5 μm over 21 orders with $R \sim 6000$. We scaled the reduced and order-stitched spectrum of B11 to the observed H-band photometry on the Maunakea Observatories (MKO) photometric system following Line et al. (2017). We will explore potential issues regarding which regions of this spectrum to include in our analysis (for example due to telluric absorption or order-stitching problems) in later sections.

We also use the low-resolution spectrum of UGPS 0722 from the SpeX Prism Library (Burgasser 2014), which covers a similar wavelength range of 0.8–2.5 μm with a wavelength-dependent resolution of ∼87–300. This spectrum was also calibrated to flux units using the same H-band photometry as for the FIRE spectrum. The flux-calibrated FIRE and SpeX spectra are shown in Figure 1.

2.2. GPU Retrieval Framework

We use the CHIMERA retrieval framework successfully applied previously to low-resolution brown dwarf spectra (Line et al. 2015, 2017; Zalesky et al. 2019). However, generating a

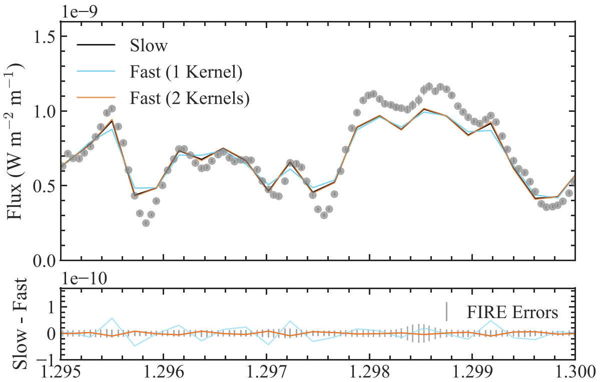

Figure 2. Comparison of different rotational broadening methods. The top panel shows modeled emission spectra using different rotational broadening methods compared to a snippet of the FIRE spectrum of UGPS 0722 shown in the gray data points. The bottom panel shows the difference between the model broadened with a wavelength-dependent kernel (“Slow”) and those using either 1 or 2 broadening kernels for the spectrum (“Fast”), and the data error bars in this region. At least two broadening kernels, using the median wavelengths of the blue and red halves of the spectrum, are required to reduce the difference with the slower, more accurate method to smaller than the error bars of the FIRE spectrum.

Table 1
Free Parameters in Our Retrieval Model

Parameter	Description
log(f_i)	log of the uniform-with-altitude volume mixing ratios of H_2O, CH_4, CO, NH_3, H_2S, Na, and K
log(g)	log surface gravity [cm s^{-2}]
$(R/D)^2$	radius-to-distance scale [R_{Jup}/pc]
T(P)	temperature at 15 pressure levels [K]
b	errorbar inflation exponent (Line et al. 2015)
γ, β	TP profile smoothing hyperparameters (Line et al. 2015)
log(Cloud VMR)	log of the cloud volume mixing ratio
log(P_c)	log of the cloud base pressure
f_{sed}	sedimentation efficiency
RV	radial velocity [km s^{-1}]
v sin i	rotational velocity [km s^{-1}]

Table 2
Opacity Sources for Our Retrieval Model

Species	Opacity Sources
H2-H2, H2-He CIA	Richard et al. (2012)
H_2O	Polyansky et al. (2018)
CH_4	Yurchenko & Tennyson (2014); Hargreaves et al. (2020; Section 3.3.2)
CO	Rothman et al. (2010); isotopologues: Li et al. (2015)
NH_3	Yurchenko et al. (2011); Coles et al. (2019; Section 3.3.2)
H_2S	Tennyson & Yurchenko (2012); Azzam et al. (2015); isotopologues: Rothman et al. (2013)
K	see Marley et al. (2021); Allard et al. (2016; Section 3.6)
Na	see Marley et al. (2021); Allard et al. (2019; Section 3.6)

forward model emission spectrum at a resolution of $R \sim 60{,}000$ (which is then binned to $R \sim 6000$) is quite computationally expensive. Thus, to make this study feasible, we must use a modified version for use with graphical processing units (GPUs), that builds upon the code described in Zalesky et al. (2022). Specifically, we modify the radiative transfer to solve the two-stream multiple scattering problem using the methods described in Toon et al. (1989). However, as we are not in a particularly cloud regime, the effects of multiple scattering are negligible. As in the previous studies done with this framework, we use the affine-invariant Markov Chain Monte Carlo (MCMC) ensemble sampler package `emcee` (Foreman-Mackey et al. 2013). We include uniform-with-altitude volume mixing ratios of H_2O, CH_4, CO, NH_3, H_2S, Na, and K, the surface gravity, a radius-to-distance scaling factor, a TP profile, and three cloud parameters: cloud volume mixing ratio, the cloud pressure base, and the sedimentation efficiency (Ackerman & Marley 2001). As in Line et al. (2017), the TP profile is parameterized by 15 independent TP points subject to two smoothing hyperparameters. These 15 TP points are interpolated onto a finer 70 layer pressure grid for the radiative transfer using a cubic Hermite spline.

The chemical species and associated opacity sources used in this work are listed in Table 2. We began with the set of absorption cross sections presented in Freedman et al. (2008) and subsequently updated as detailed in Freedman et al. (2014), Lupu et al. (2014), and Marley et al. (2021). However, we use a set of H_2O opacities calculated based on the POKAZATEL line list (Polyansky et al. 2018). In Section 3, we explore the effect of switching our opacity source for a number of species, including NH_3 (Coles et al. 2019), CH_4 (Hargreaves et al. 2020), K (Allard et al. 2016), and Na (Allard et al. 2019). For the cloud opacity, we used Mie scattering theory assuming an Mg_2SiO_4 cloud with optical properties from Wakeford & Sing (2015). However, the exact cloud species assumed should not particularly matter as cloud optical properties tend to be gray over these near-infrared wavelengths and the cloud’s placement and extent in the atmosphere are parameterized independent of composition.

At these moderate resolutions, we add the radial and rotational velocities present in the spectrum as two additional parameters in the retrieval forward model. Both properties were measured in B11 by comparison to grid models. We use the *dopplerShift* function from PYASTRONOMY (Czesla et al. 2019) to shift the forward modeled emission spectrum by a given radial velocity and interpolate it back onto the input wavelength grid.

For the rotational velocity, we first tested the *rotBroad* function from PYASTRONOMY, which implements rotational broadening as described by Gray (2008) for a given v sin i and linear limb-darkening coefficient (we chose 0). This function convolves the modeled spectral lines with a wavelength-dependent line profile representing the Doppler line broadening from rotation, called the “broadening kernel.” However, this method proved unfeasibly slow, requiring 89 s to generate one broadened forward model spectrum. We then tested the *fastRotBroad* function from PYASTRONOMY, which uses a single broadening kernel that only depends on the median wavelength of the input data, leading to a much faster forward model generation time of 0.19 s but differences with the slower version that were larger than the error bars of the FIRE spectrum, as shown in Figure 2. As a compromise, we split our

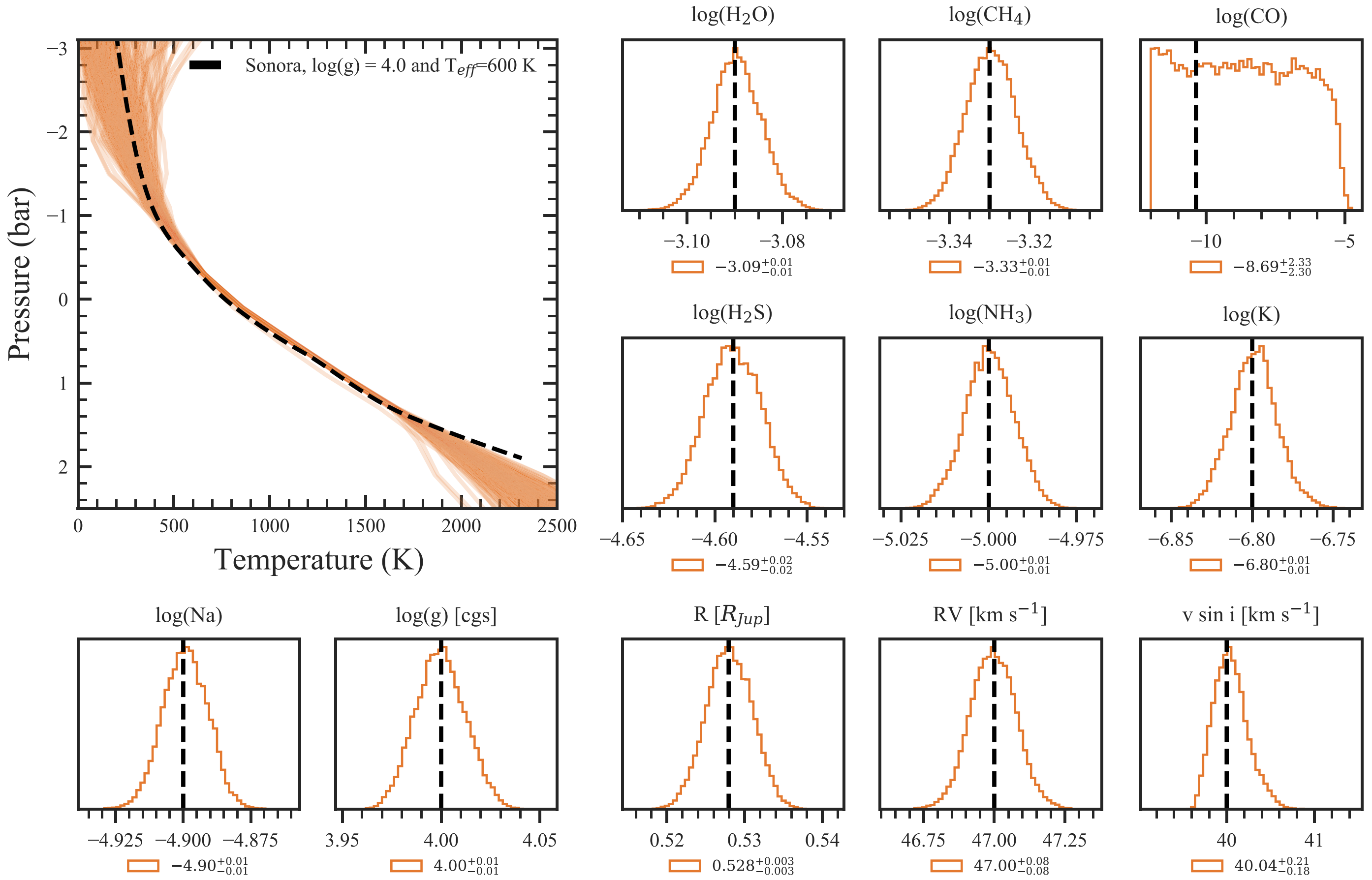

Figure 3. Retrieved TP profiles and posteriors of certain parameters for a “fake” FIRE spectrum based on the Sonora Bobcat model with an effective temperature of 600 K and surface gravity log(g) = 4.0.

spectrum into two and used *fastRotBroad* for each half, taking 0.2 s but leading to differences from the more accurate function that were smaller than the error bars.

To test how our retrieval framework might perform on the FIRE data of UGPS 0722, we generated a fake test data set. We used CHIMERA to create one forward model based on the TP profile from the Sonora Bobcat grid (Marley et al. 2021) for an object with $T_{eff} = 600$ K and $\log(g) = 4.0$, giving it a radial velocity of 47 km s^{-1} and a v sin i of 40 km s^{-1}. We assume constant-with-altitude chemical abundances with log volume mixing ratios of $H_2O = -3.09$, $CH_4 = -3.33$, $CO = -10.37$, $H_2S = -4.59$, $NH_3 = -5.00$, $K = -6.80$, and $Na = -4.90$. This forward model was convolved to the FIRE instrument resolution, interpolated onto the wavelength grid of the FIRE spectrum, and given the same error bars as the FIRE spectrum of UGPS 0722. As such, we assume an $(R/D)^2$ value of 0.0158 (corresponding to a radius of $\sim$0.528 $R_{\rm Jup}$ for an object at the distance of UGPS 0722), which is needed to give the same peak-flux-to-error ratio as the FIRE spectrum of UGPS 0722. The results from a CHIMERA retrieval on this test data set compared to the input values are shown in Figure 3. We see that we are able to recover the input values with high accuracy and precision (with the exception of CO as it is unconstrained due to the low input mixing ratio), particularly with an unprecedented uncertainty of $\sim$0.01 dex on the chemical abundances and surface gravity, $\sim$10× more precise than constraints from spectra at $R \sim 100$ (Line et al. 2017; Zalesky et al. 2022).

3. Results

3.1. Initial Fire Retrieval versus SpeX

Initially, we used the entire order-stitched and flux-calibrated FIRE spectrum of UGPS 0722, with a few spurious data points effectively ignored by greatly inflating their error bars. However, in regions of high telluric absorption, the error bars on the spectrum were artificially underestimated (almost 14 orders of magnitude more precise than elsewhere). To prevent these data points from incorrectly driving our results, the error bars in these regions are inflated to a high enough value that these data points functionally do not contribute to our retrieval analysis. We also mask out those regions of strong telluric absorption in the SpeX spectrum as well to allow for a direct comparison.

Figure 4 shows the retrieved TP profiles and posterior distributions for selected parameters from our initial analysis of the UGPS FIRE spectrum compared to results from the SpeX spectrum. Though the FIRE spectrum potentially offers more precision than the SpeX results, we find our MCMC chains have trouble converging, with bimodal posteriors, unphysical values for certain parameters like the surface gravity, and very jagged TP profiles.

We suspected our forward model was too flexible, which was leading to overfitting and unphysical results. We reduced the number of parameters in our model by fixing the second TP profile smoothing hyperparameter β and the cloud parameters to specific values. Line et al. (2017) found letting β vary had a

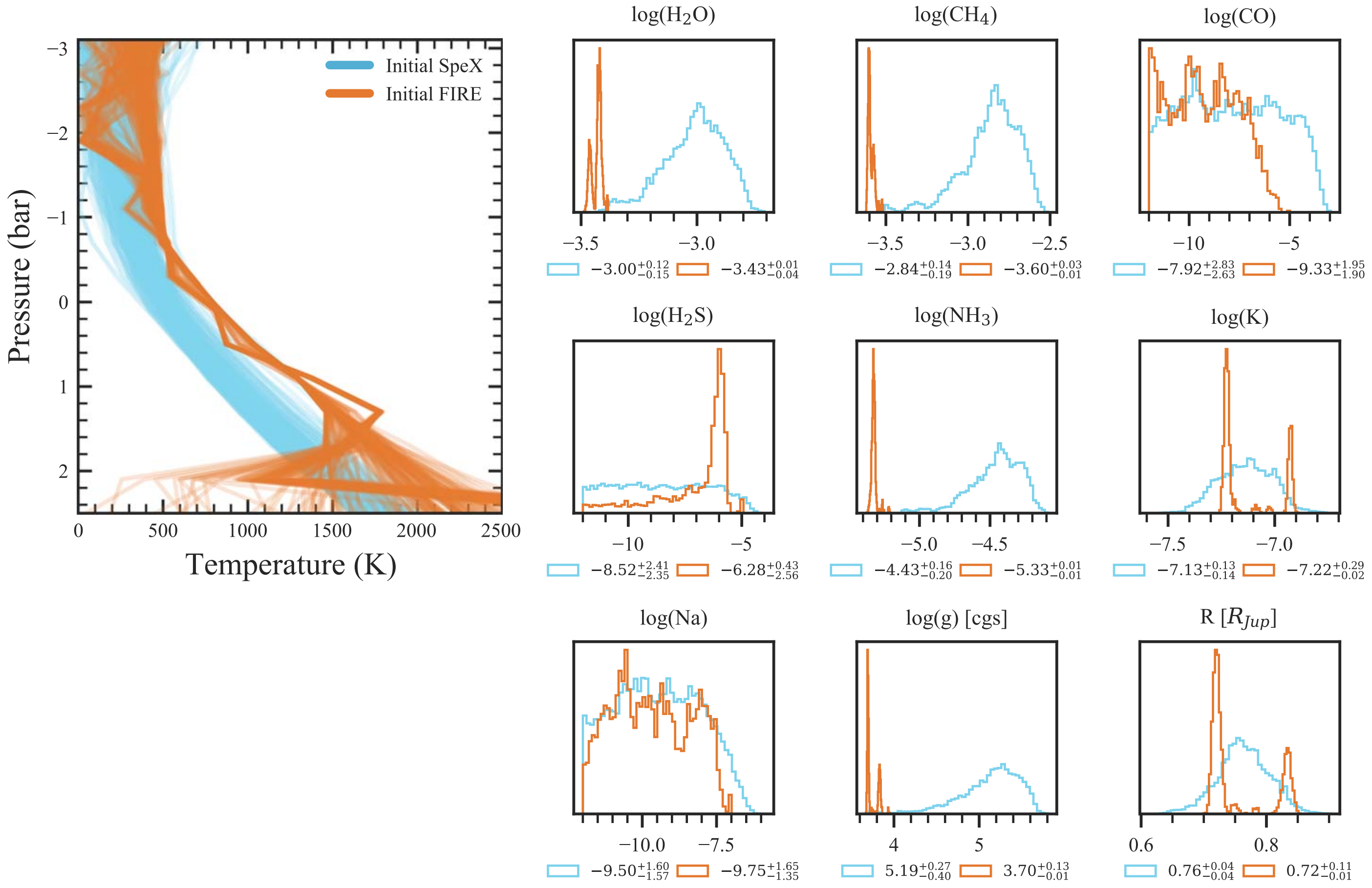

Figure 4. Retrieved TP profiles and posterior distributions for selected parameters for initial retrievals on the SpeX and FIRE spectra of U0722.

negligible effect compared to the nominal fixed value of $\beta = 5 \times 10^{-5}$ used by Line et al. (2015). As previous work (Line et al. 2015, 2017) showed little evidence for optically thick clouds on T dwarfs, we set the cloud opacity parameters [log(Cloud VMR), log(P_c), $f_{\rm sed}$] = [−15, 2, 10], consistent with an optically thin cloud deck.

The effect of fixing β and the cloud parameters is shown in Figure 5 in orange. The TP profiles are smoother and more precisely constrained, while we no longer see bimodal posteriors for the plotted parameters. We note a potential detection of H_2S in this object, although the posterior on the H_2S abundance has a long lower tail. We will explore letting the cloud parameters vary again in Section 3.8.

3.2. Effect of Resolution Element and Wavelength Limits

Next, we decided to mimic more the analysis of B11 and limit the FIRE spectrum to 0.9–2.35 μm when comparing to models, effectively getting rid of the noisiest regions of the spectrum at the beginning and end. Additionally, like SpeX, the FIRE spectrum is oversampled compared to a spectral resolution element, so we take every fourth pixel of the spectrum to ensure independent data points (e.g., Line et al. 2017; Kitzmann et al. 2020).

Figure 5 shows the effect of these two changes in gray. While the retrieved TP profiles are very similar to the previous results at pressures less than ∼15 bars, the deep atmosphere is much warmer. The molecular abundances often shift slightly, but with the exception of H_2O the new posteriors are within 1σ. Our precision on almost all parameters also decreases, due to the substantial decrease in the number of included data points.

3.3. Effect of Updated Line Lists

In an effort to improve our best model fit to the observed spectrum, we investigated the effect of changing the sources of line lists used for CH_4 and NH_3. For NH_3, we upgraded to the more recent CoYuTe (Coles et al. 2019) ExoMol line list instead of the older BYTe (Yurchenko et al. 2011) list we were using previously. For CH_4, we replaced the ExoMol 10to10 list (Yurchenko & Tennyson 2014) with the recent HITEMP line list published by Hargreaves et al. (2020), who combined the more accurate ab initio line lists of Rey et al. (2017) with HITRAN2016 data (Gordon et al. 2017).

Comparisons of these "old" and "new" line lists for CH_4 and NH_3 at a specific pressure and temperature are shown in Figure 6. The two CH_4 opacities on the left show clear deviations beyond just shifts to line positions, especially blueward of ∼1.62 μm. Hargreaves et al. (2020) demonstrate the better match of their CH_4 line list to experimental data for this wavelength region than the ExoMol CH_4 line list. In contrast, while minor differences are evident between the two NH_3 line lists in the right panel, they have similar overall values across the wavelength region of the spectrum. The effect of these changed line lists on our retrieved parameters is discussed below.

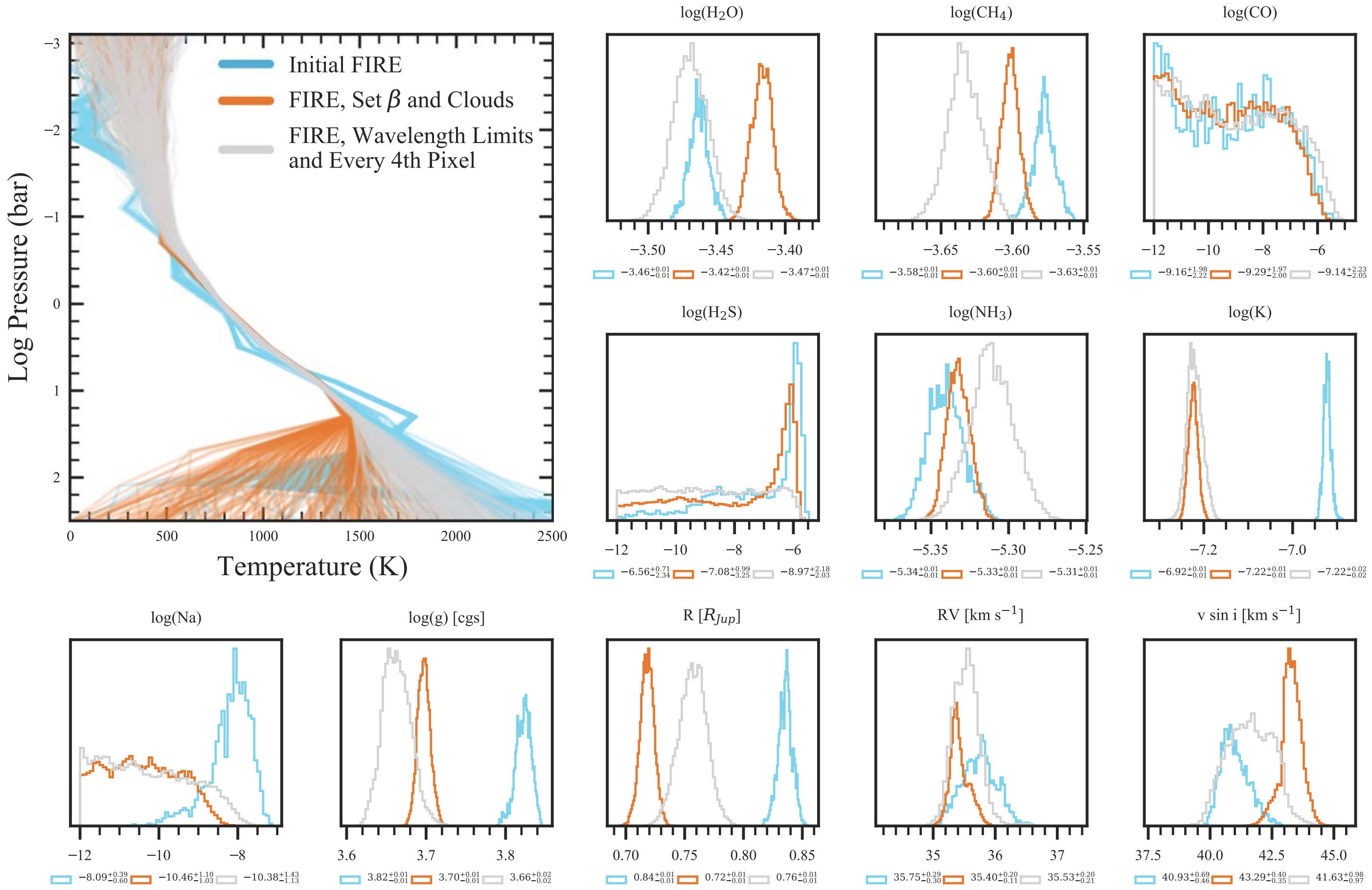

Figure 5. Effect on the retrieved TP profiles and selected posteriors of fixing the smoothing hyperparameter β and cloud parameters to set values (orange). In Section 3.2, we then limited the input spectrum to 0.9–2.35 μm and took every fourth pixel to limit the analysis to one data point per resolution element (gray).

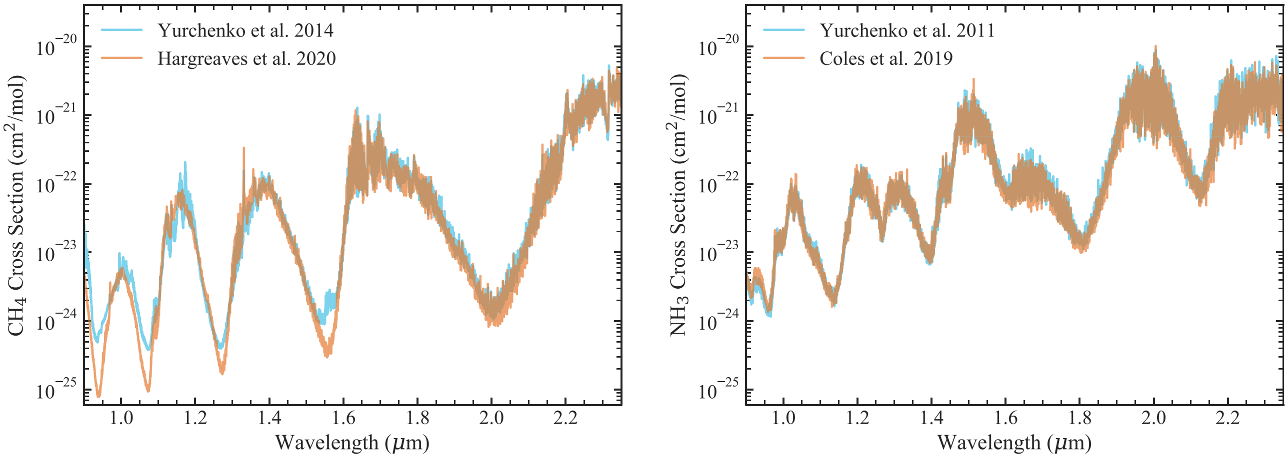

Figure 6. Comparison of old and new molecular cross sections at 725 K and 1 bar, and smoothed to $R \sim 6000$. Left: comparison of CH$_4$ cross sections from the ExoMol 10to10 (Yurchenko & Tennyson 2014) and HITEMP (Hargreaves et al. 2020) line lists. Right: comparison of NH$_3$ cross sections from the older BYTe (Yurchenko et al. 2011) and newer CoYuTe (Coles et al. 2019) ExoMol line lists.

3.3.1. Low-resolution Retrievals

Figure 7 shows the effect of these updated line lists on the retrieved TP profile and selected posteriors for the SpeX spectrum. The retrieved TP profiles are consistently warmer than those obtained when using the Yurchenko & Tennyson (2014) CH$_4$ and Yurchenko et al. (2011) NH$_3$ line lists. Constraints on the abundances of H$_2$O, CH$_4$, and NH$_3$ all shift to lower values, while the retrieved abundance of K increases by ∼0.5 dex. The retrieved surface gravity also decreases, from $\log(g) = 5.19^{+0.27}_{-0.40}$ to $\log(g) = 4.43^{+0.27}_{-0.17}$ (cgs). Furthermore, the retrieved radius, assuming a parallax distance of 4.12 ± 0.04 pc (Leggett et al. 2012), decreases from $0.76^{+0.06}_{-0.04}$ to $0.5^{+0.03}_{-0.02}$ $R_{\rm Jup}$, an unphysically small value (see Section 4.1 for further discussion). Notably, the dramatic decreases in both surface

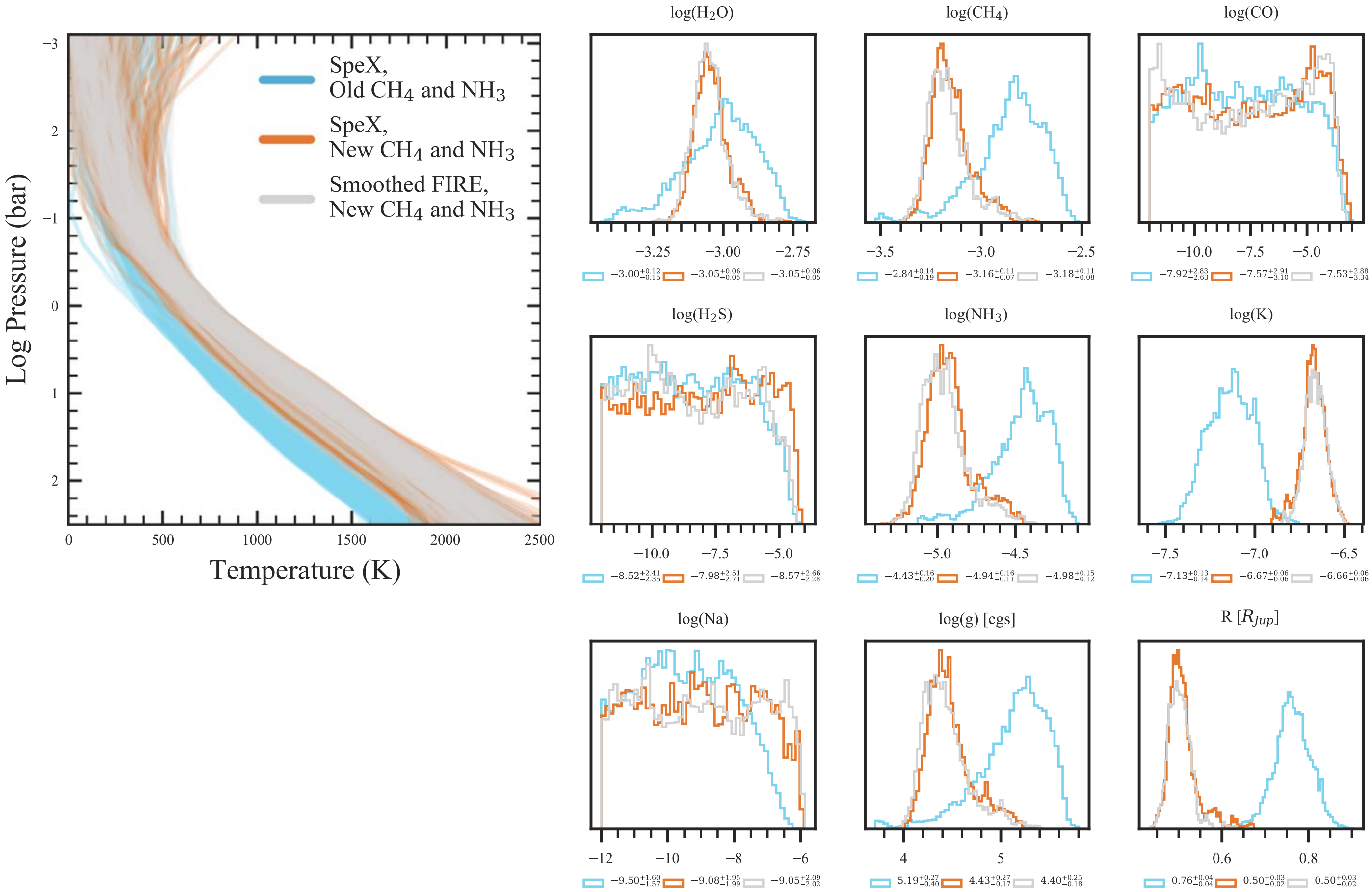

Figure 7. Effect on the retrieved TP profiles and selected posteriors of updating the CH_4 and NH_3 line lists to those of Hargreaves et al. (2020) and Coles et al. (2019), respectively, for the SpeX spectrum (orange). Results for the FIRE spectrum smoothed to the resolution of SpeX (gray) agree well for all parameters with those from the SpeX spectrum.

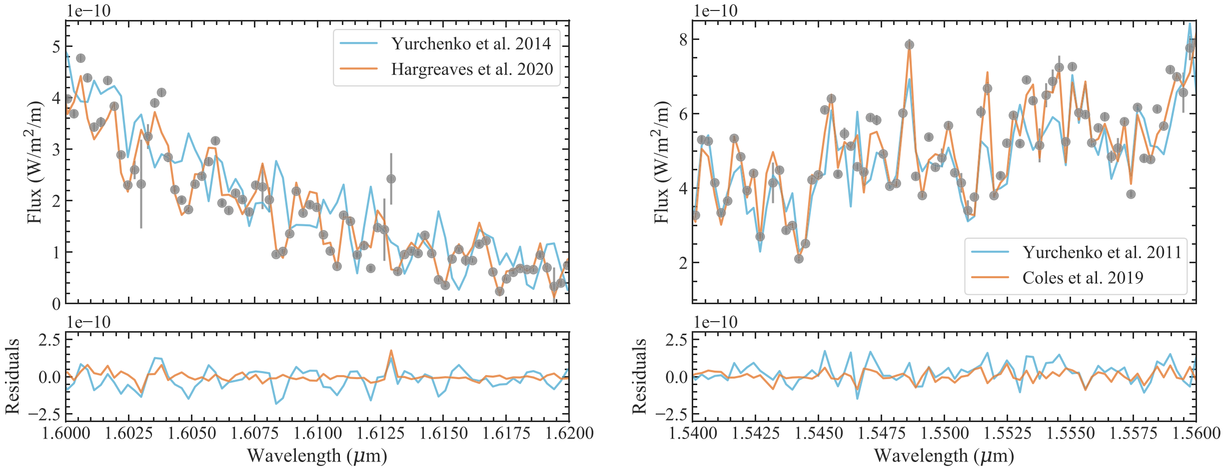

Figure 8. Comparisons of median model spectra for retrieval results using old and new molecular line lists, compared to the FIRE spectrum of U0722 in narrow regions of the spectrum where CH_4 and NH_3 are expected to dominate on the left and right, respectively. Left: models with the Yurchenko & Tennyson (2014) and Hargreaves et al. (2020) CH_4 line lists; the Hargreaves et al. (2020) line list does a significantly better job at matching the CH_4 lines in this region. Right: models with the Yurchenko et al. (2011) and Coles et al. (2019) NH_3 line lists; the Coles et al. (2019) line list improves the fit to NH_3 lines in this region.

gravity and radius are driven by updating the CH_4 line list, as this effect occurs even when the NH_3 line list is kept the same.

To assess if the FIRE data set is consistent with the SpeX spectrum, we smoothed and sampled the FIRE data down to the SpeX resolution. Our retrieval results on this smoothed FIRE spectrum are compared to the original SpeX results (both with the updated cross sections) in Figure 7. The retrieved constraints arising from the smoothed FIRE spectrum and the SpeX spectrum show remarkable agreement. This suggests that at low resolutions, observations at different times with completely different instruments produce extremely consistent results, given our retrieval model assumptions.

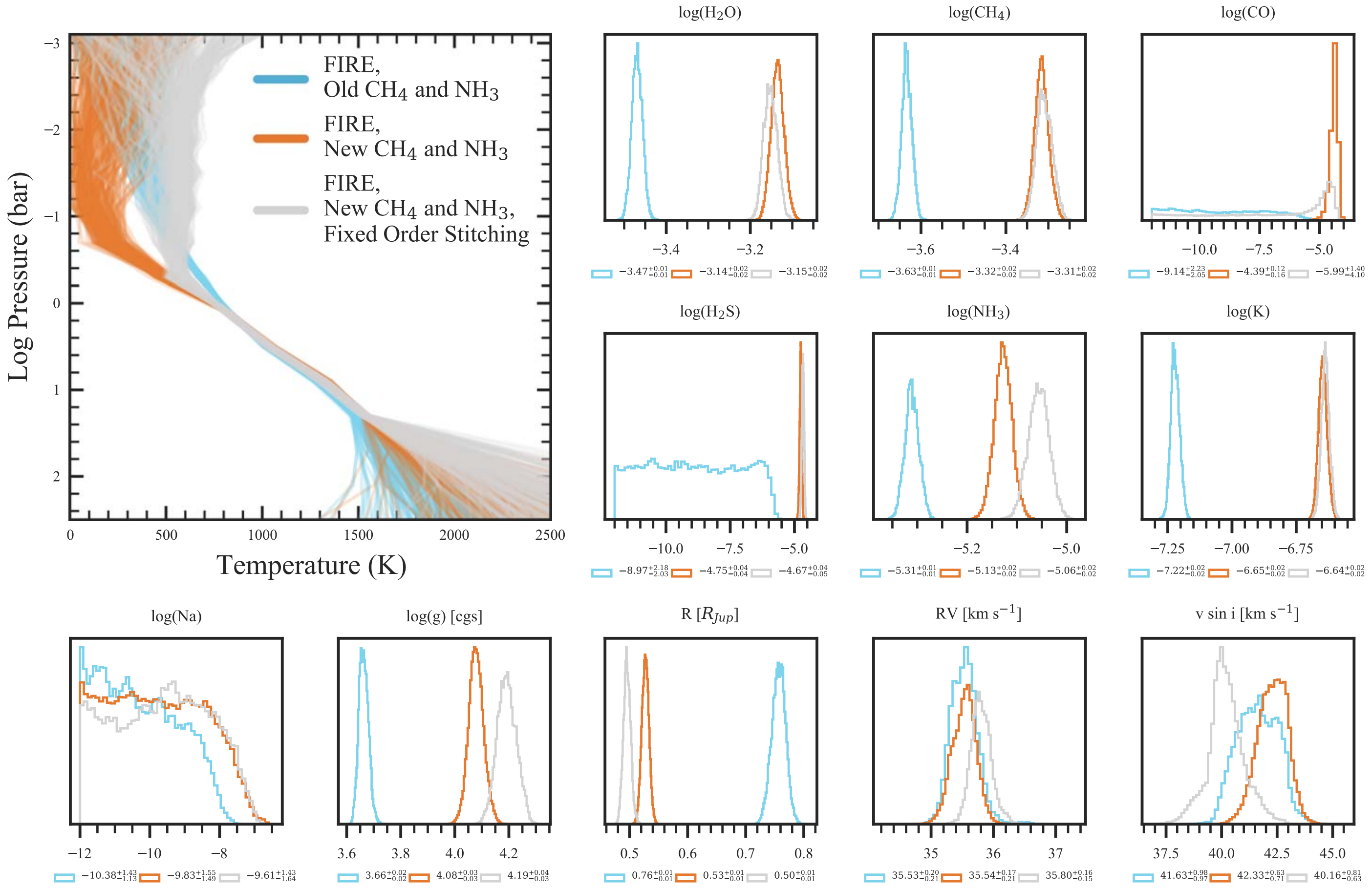

Figure 9. Effect on the retrieved TP profiles and selected posteriors from the FIRE spectrum when updating the CH4 and NH3 line lists to those of Hargreaves et al. (2020) and Coles et al. (2019), respectively (orange). The retrieved TP profiles and selected posteriors resulting from removing regions of the data where order stitching was not successful (Section 3.4) are shown in gray.

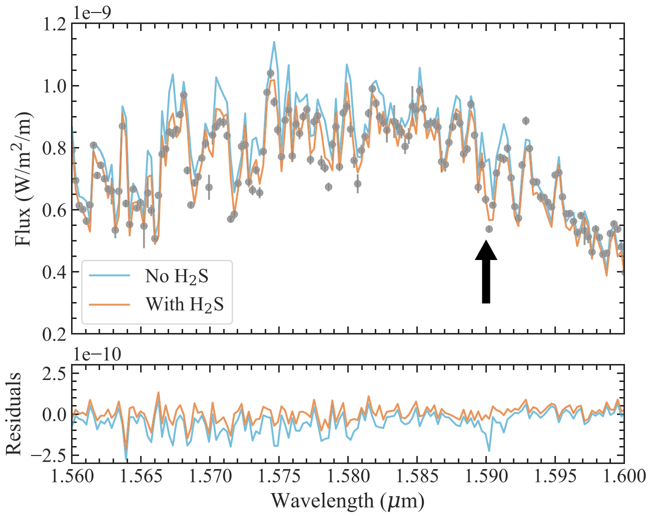

Figure 10. Model spectrum from the median retrieved parameters generated with (orange) and without (blue) H_2S, compared to a snippet of the FIRE spectrum where H_2S opacity is expected. Some features are better fit with the inclusion of H_2S. The black arrow indicates a blended H_2S line consistent with the H_2S detection of Tannock et al. (2022).

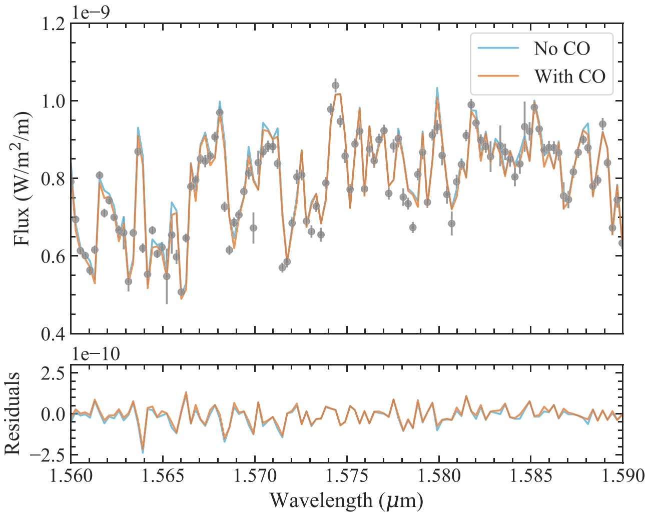

Figure 11. Model spectrum from the median retrieved parameters generated with and without CO, compared to a snippet of the FIRE spectrum where some CO opacity is expected. While including CO does slightly improve the fit to the data, the effect is slight.

3.3.2. Medium-resolution Retrievals

With the increased spectral resolution of FIRE, we can better assess the accuracy of the line positions in various line lists. Figure 8 shows two narrow regions of the FIRE spectrum of U0722 where CH_4 and NH_3 are dominant in the left and right panels, respectively. For each molecule, we show the model spectra generated with the updated line lists. In both cases, our newer line lists are better able to replicate the line positions of their respective molecules. Both the Hargreaves et al. (2020) and Coles et al. (2019) line lists incorporated empirical energy levels where available, as opposed to solely computed ones, leading to improved line position accuracy.

Unsurprisingly, improving the fit to line positions in our model does affect our retrieved atmospheric parameters. Figure 9 shows how updating the line lists of CH_4 and NH_3 affects our retrieved TP profiles and posteriors in orange. While the TP profiles are relatively similarly deeper than ∼1 bar, the scenario with updated line lists prefers the atmosphere to be as cold as possible around 0.2 bars. Our retrieved posteriors for all molecular abundances as well as potassium do shift to higher values. The surface gravity also increases, from a median log $(g) = 3.66\ ^{+0.02}_{-0.02}$ to $\log(g) = 4.08\ ^{+0.03}_{-0.03}$(cgs), a more plausible value. However, the radius decreases just like for the SpeX retrieval in Section 3.3.1, from $0.76^{+0.01}_{-0.01}$ to $0.53^{+0.01}_{-0.01}\ R_{\rm Jup}$, an unphysically small size, which we discuss more in Section 4.1. The retrieved radial velocity and $v \sin i$ are relatively unaffected by our choice of CH_4 and NH_3 line lists, indicating these measurements may be primarily driven by H_2O lines in the spectrum.

Notably, we retrieve bounded constraints on the H_2S and CO abundances; the CO constraints were unbounded when using the older line lists. Figure 10 shows model spectra for the median retrieved parameters, with and without H_2S, where we expect the H_2S opacity to have an effect. Both H_2S and CO have the greatest effect on our model spectra between ∼1.56–1.60 μm where there is a window in the combined opacity of H_2O and CH_4. Including H_2S does improve the model fit in this region of the spectrum, but mostly as an overall shift in the strength of features. However, around 1.59 μm there is what appears to be an H_2S line that is blended with another feature but clear in the residuals shown on the bottom. Tannock et al. (2022) reported an H_2S detection in a high signal-to-noise, $R \sim 45{,}000$ spectrum of a T6 dwarf, where they show a strong H_2S feature at this exact location around 1.59 μm. Thus, our constraint on the H_2S abundance is consistent with this feature, though it is dependent on a relatively small number data points (∼three points for the 1.59 μm feature and ∼20 others). Figure 11 shows models with and without CO, for the region of the spectrum where the model spectra are most different from each other. While the inclusion of CO does improve our model fit in this region, there is not a clear CO feature to point to as the source of our CO constraint. Thus, while we do have a bounded posterior for the CO abundance, it is perhaps a less trustworthy detection.

3.4. Issues with Order Stitching

FIRE observations in cross-dispersed mode are spread over 21 different orders. These orders have some overlap in wavelength coverage on either end. The final stitched spectrum published by B11 combined these orders into a single spectrum by averaging the regions where the orders overlapped. However, in some cases when one order was noisier than the other, this averaging can lead to data artifacts. We first noticed this issue when inspecting the spectrum around 2.1 μm, where a jump or step in the data appears that is not possible to reproduce with our forward models, as shown in the top panel of Figure 12. Additional examples of overlapping regions potentially subject to order-stitching problems are shown in the lower two panels. While neither panel shows a step similar to the one seen at 2.09 μm, both cover regions where there is substantial disagreement between the two component orders leading to perhaps unphysical features in the stitched spectrum, particularly toward the middle of the overlapping areas.

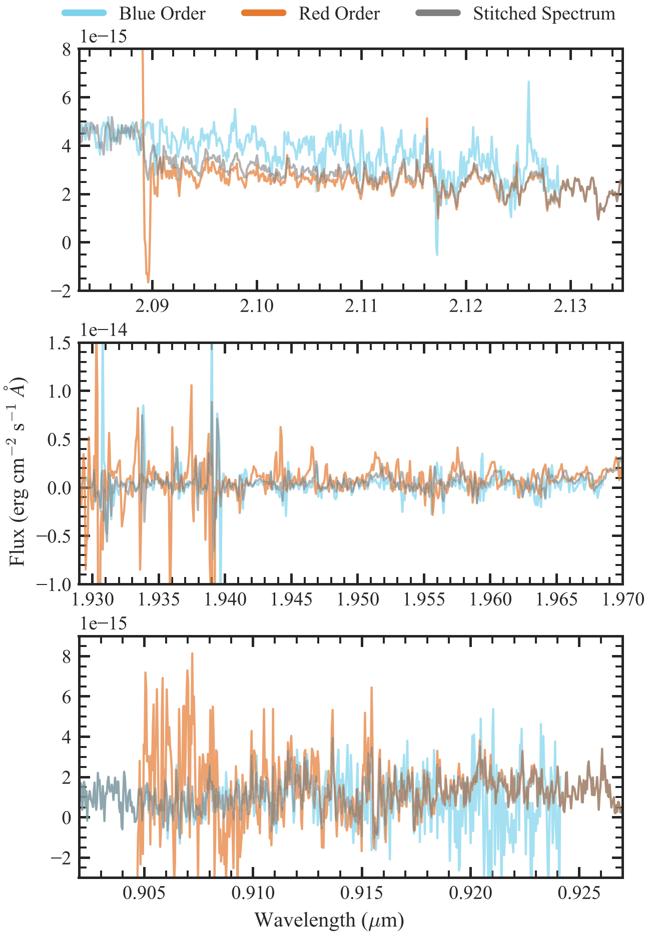

Figure 12. Example order-overlap regions of the stitched FIRE spectrum (gray) that were removed due to issues with order stitching, compared to the component orders (blue and orange).

To avoid these potential order-stitching issues from biasing our retrieved results, we artificially inflated the error bars in order-overlap regions where the final stitched product differed from either input order spectrum by more than 10%, effectively removing these data points from our analysis. Figure 9 shows the result of removing these order-stitching artifacts on our retrieval results in gray. Though the region of the atmosphere shown in Figure 12 is near the peak of the K band and thus probes hotter parts of the atmosphere, other problematic order-overlap regions masked by this process were on the edges of peaks in the spectrum and therefore contributed spuriously to constraints on the TP profile of the upper atmosphere. Our molecular and alkali abundances change slightly, with a less precise constraint on the amount of CO. While our median retrieved surface gravity increases to a slightly more plausible value of $\log(g) = 4.19\ ^{+0.04}_{-0.03}$ from $\log(g) = 4.08\ ^{+0.03}_{-0.03}$(cgs), our median radius shrinks even more to $0.50^{+0.01}_{-0.01}\ R_{\rm Jup}$. Finally, our retrieved radial velocity and $v \sin i$ posteriors also slightly shift as well.

3.5. Retrieving on Subsections of the Spectrum

While our stitched FIRE spectrum of U0722 covers the y–K bands, we wanted to investigate the constraining power of

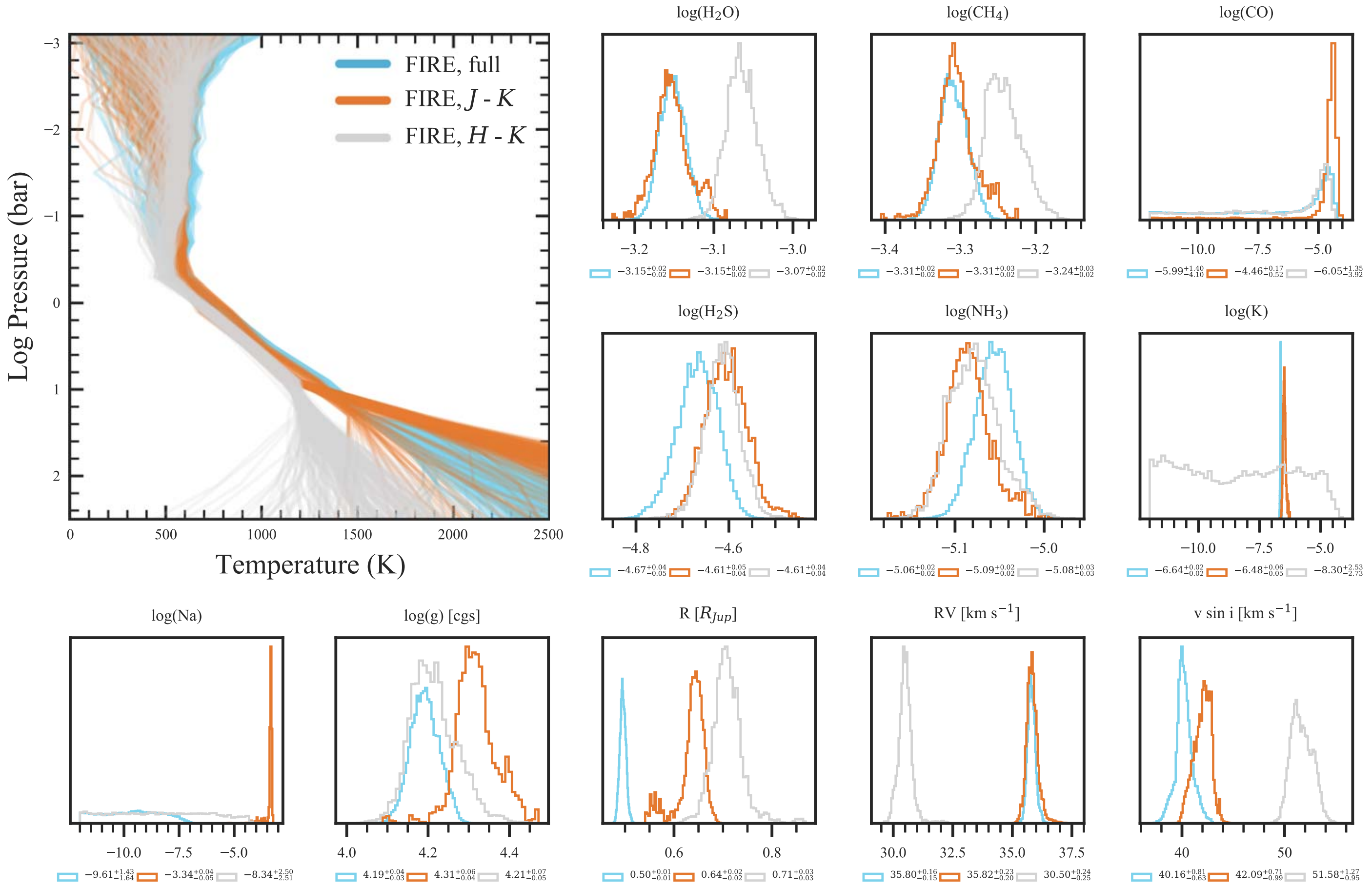

Figure 13. Effect on the retrieved TP profiles and selected posteriors when performing the retrieval on the full wavelength range, *J*–*K*, or just the *H* and *K* bands.

different sets of spectral bands. In particular, Hargreaves et al. (2020) retains the completeness limits of the input line lists from Rey et al. (2017), giving a temperature-dependent maximum wavenumber limit for which the CH_4 line list can be considered complete, or including all lines strong enough to affect the resulting opacity. This limit is 10,700 cm^{-1} or 0.93 μm for 1300 K, and 9500 cm^{-1} or 1.05 μm for 1400 and 1500 K. Thus, the Hargreaves et al. (2020) CH_4 line list is not complete for the deeper, hotter temperatures probed by the *y* band. Motivated by this potential completeness problem, we retrieved on the *J*–*K* band data only, followed by a retrieval on solely the *H*–*K* bands.

Comparisons of the retrieved TP profiles and select posteriors are shown in Figure 13. The TP profiles get cooler as the shorter-wavelength data are progressively removed from the analysis. As the flux in the *y* and *J* bands comes from deeper in the atmosphere, we do not constrain the temperatures to as deep of pressures without these data, as indicated by the “fanning out” of the TP profiles in these deeper layers. The H_2O and CH_4 abundances shift to higher values when just looking at the *H* and *K* bands. While our constraint on the CO abundance becomes more precise for the *J*–*K* retrieval, there is still a long tail toward low values. The H_2S and NH_3 posteriors shift slightly with the exclusion of the *y*-band data. While we lose all constraints on the K abundance for just the *H* and *K* bands, we have a very precise and high constraint on the Na abundance when looking at the *J*–*K* bands. Our retrieved surface gravity is also higher for the *J*–*K* retrieval than the other two, with a median of $\log(g) = 4.31^{+0.06}_{-0.04}$. We retrieve a larger radius as we remove each bluer band of data, perhaps reflecting the cooler TP profiles retrieved for these cases as well. Finally, removing the *J*-band data causes quite a shift in the retrieved radial velocity and $v \sin i$ values, pointing to the importance of the strong water lines in the *J* band to our constraints on these values for the full spectrum.

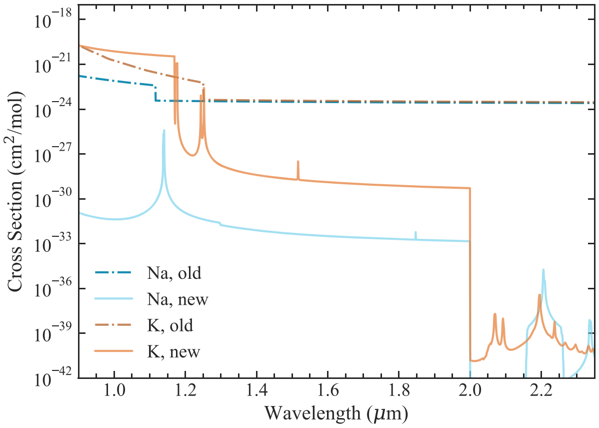

Figure 14. Comparison of old (dashed–dotted) and new (solid) alkali cross sections at 725 K and 1 bar, and smoothed to $R \sim 6000$. The older alkali cross sections are from Freedman et al. (2014), while the newer ones are based on Allard et al. (2016) and Allard et al. (2019) for K and Na, respectively.

Given that the Hargreaves et al. (2020) line list is not complete for the *y* band at the temperatures found in this object, the *J*–*K* retrieval is perhaps a compromise between CH_4 line completeness while retaining some flux from deeper in the

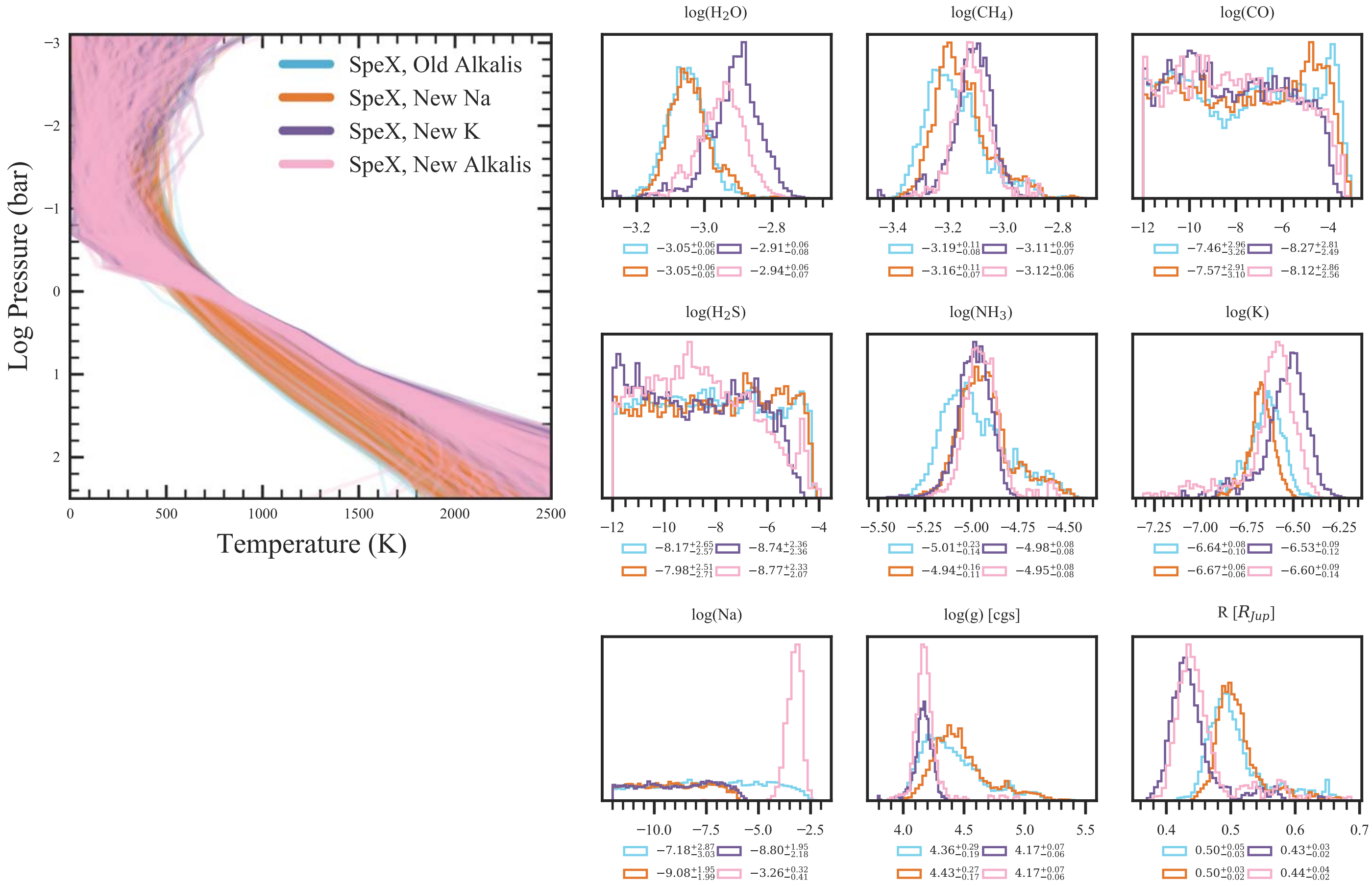

Figure 15. Effect of updating the alkali cross sections on the retrieved TP profiles and selected posteriors using the SpeX spectrum.

atmosphere. However, the anomalously high Na abundance does call into question the physical plausibility of these results.

3.6. Effect of Alkali Opacities

Another change we made to our framework was to update the opacities used for the alkali metals Na and K. In particular, their strong lines at ∼0.59 and 0.77 μm can be very broadened and significantly impact the near-infrared spectrum of a brown dwarf. Prescriptions for these line profiles can vary quite a bit. We first used older alkali opacities based on the unified line-shape theory (Allard et al. 2007a, 2007b), as used in the Sonora Bobcat grid (Marley et al. 2021); example cross sections of Na and K for 725 K and 1 bar are shown in Figure 14, which basically become flat-continuum opacity sources after a certain wing cutoff point. The high retrieved Na abundance for the *J*–*K* retrieval in Section 3.5 above can then be understood as an additional source of continuum opacity used to reduce the *J*-band flux, which is not penalized when the *y* band is excluded. These alkali opacities were shown by Gonzales et al. (2020) to produce more physically reasonable alkali abundances in their retrieval study of a d/sdL7+T7.5p binary than those from Burrows & Volobuyev (2003). In contrast, newer cross sections based on the recent theoretical advancements of Allard et al. (2016, 2019) have more complicated shapes and significantly lower cross sections redward of ∼1.2 μm.

These differences demonstrated in Figure 14 between the older and newer line profiles can greatly affect our retrieved parameters. To isolate the differences, we retrieved on the SpeX data with just updating the Na cross sections, just updating K, and then updating both simultaneously. The retrieved TP profiles and selected posteriors for the different alkali treatments for the SpeX data are shown in Figure 15. Updating the Na opacity on its own does not particularly affect our retrieved results, perhaps unsurprisingly since the older K cross sections have so much more opacity. Updating to the new K causes a large change to our retrieved TP profiles, causing a very cold upper atmosphere with an inversion and a hotter, more precisely constrained profile from ∼1–10 bars. The retrieved surface gravity and radius also decrease. Finally, updating Na and K at the same time is mostly similar to when just using the new K, except for a very high amount of retrieved Na.

Figure 16 shows the effect of updating the alkali cross sections on our retrieved TP profiles and posteriors of selected parameters for the FIRE data of U0722. Similar to the SpeX retrieval, the retrieved TP profile is hotter from ∼1–10 bars and goes to 0 K (unphysical) at ∼0.1 bars before inverting back to higher temperatures. The abundances of many species shift to higher values, particularly Na, which again has an extremely high abundance. Additionally, the CO posterior loses its long, low tail, leading to a higher median abundance. We also retrieve a lower surface gravity, concordant with the SpeX results, while the radius increases slightly.

Looking at a spectrum generated with the median retrieved parameters compared to one with significantly less Na, we see that the only discernible differences occur from ∼0.9–0.98 μm, shown in Figure 17. The gaps in the FIRE data shown were

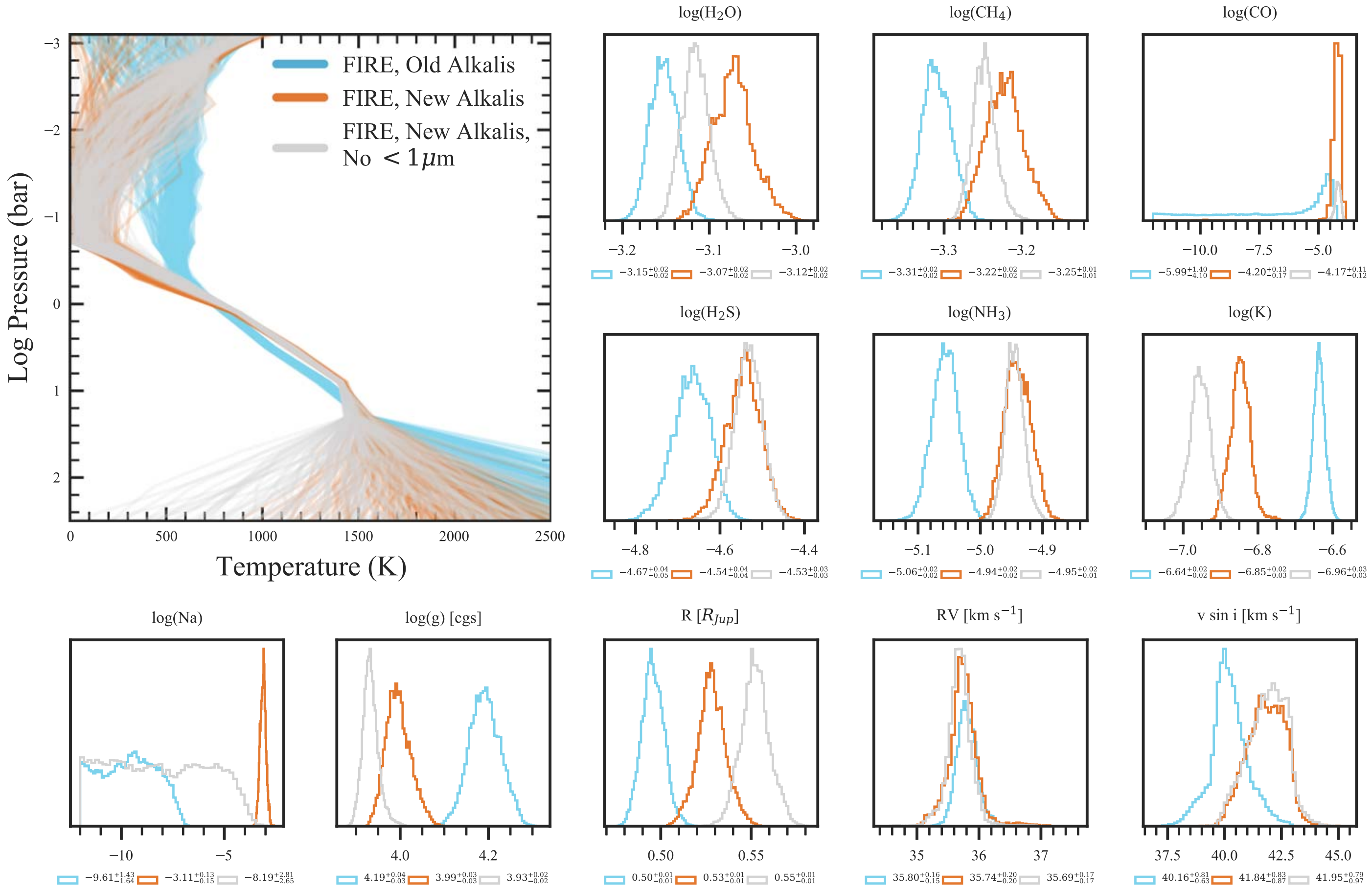

Figure 16. Effect on the retrieved TP profiles and selected posteriors for the FIRE spectrum when updating our alkali cross sections (orange). As our Na constraint appears to be only from a small snippet on the blue end of the FIRE spectrum, removing any data <1 μm leads to an unconstrained Na abundance (gray).

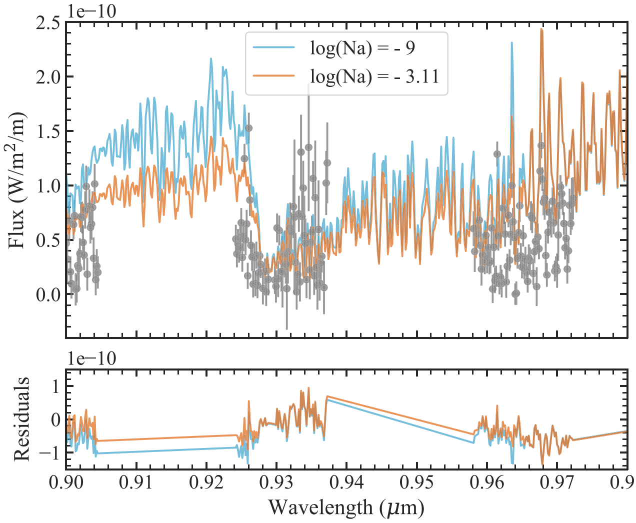

Figure 17. Model spectra from the median retrieved parameters, both using the new alkali cross sections, generated with and without the retrieved high Na abundance. This wavelength region is the only one where the increased Na abundance leads to a notable difference in the model spectra.

regions where order stitching was found to be an issue as discussed in Section 3.4. Although the high Na model does get closer to fitting the data in this region, it is still not a particularly good fit by eye, completely missing many of the data points. Furthermore, this is one of the noisiest regions of the data. Thus, the high retrieved Na abundance is likely a spurious result driven by low signal-to-noise data in these regions.

We ran another retrieval on the FIRE data with the new alkali cross sections, but without any data blueward of 1 μm. The results are shown in Figure 16. The previous high Na constraint disappears as expected. While other posteriors shift as well, the constraints on the other species change only slightly. However, the inverted TP profile and even lower surface gravity compared to the retrieval with the old alkali cross sections are a cause for concern. Therefore, the old alkali cross sections are preferred as they give us more physical results. Further studies of the alkali line profiles and their effect on retrievals in particular would help provide context for these results and guidance for future medium-resolution retrievals.

3.7. Setting the Radius to One Jupiter Radius

Given the unphysically small retrieved radius for U0722, we explored the impact of fixing the retrieved radius to one Jupiter radius on the TP profile and abundance constraints. Figure 18 shows the retrieved TP profiles and selected posteriors with this fixed radius in orange compared to when the radius is allowed to vary for the retrieval described in Section 3.4. The retrieved TP profiles overlap with the previous results for ∼2–4 bars but with a slightly different slope, as they are hotter above and cooler below this region. All abundance posteriors shift, including the disappearance of the long, low tail for CO, except for H_2S, which remains relatively unchanged. In

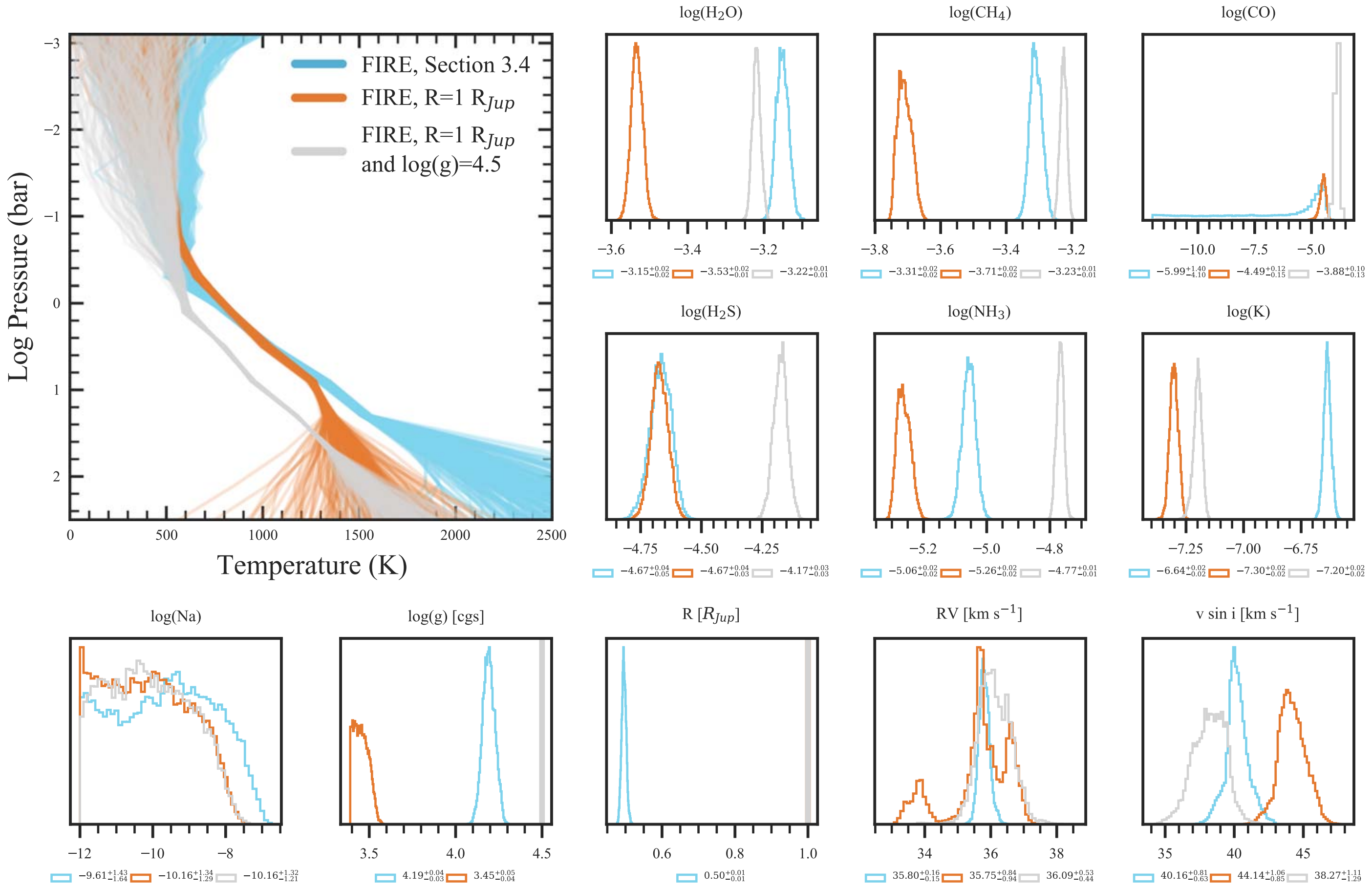

Figure 18. Effect on the retrieved TP profiles and selected posteriors of fixing the radius to 1 $R_{\rm Jup}$ (orange), and then setting the surface gravity to $\log(g) = 4.5$ as well. Almost all parameters are significantly affected.

particular all abundance shifts are to lower values, perhaps balancing out the cooler temperatures in the deep atmosphere where the flux in the y and J bands originates. The radial velocity posterior is strangely trimodal; however, one peak does correspond to the previous value. The v sin i posterior does shift as well. Importantly, the surface gravity decreases to an unphysically small median value of $\log(g) = 3.45$. Figure 28 in the Appendix shows the correlations between parameters for the retrieval discussed in Section 3.4. Gravity is notably positively correlated with the abundances of major absorbers (H_2O, CH_4, and NH_3) as well negatively correlated with the radius (through the scaling factor $(R/D)^2$). As gravity increases, the column optical depth decreases, leading to more flux particularly in the peak of each band (see Figure 2 of Line et al. 2015). Therefore, when the radius is fixed to the larger value of 1 $R_{\rm Jup}$, the retrieval converges on a smaller gravity value to balance out the increase in flux (which is also consistent with the lowered abundances). Due to this questionably low surface gravity, we do not use this fixed radius retrieval to compare to the SpeX and grid models in Section 4.

We next considered fixing the surface gravity simultaneously with the radius, choosing $\log(g) = 4.5$ consistent with a recent grid model study of U0722 (Leggett et al. 2021). The resulting TP profile and posteriors are shown in Figure 18 in gray. Since the gravity can no longer be decreased to account for the increased flux from a 1 $R_{\rm Jup}$ object, the retrieved TP profile is significantly colder than the other two plotted retrievals for the entire region of the atmosphere where it is well constrained, about 0.5 to 50 bars. We will compare this TP profile to grid model predictions in Section 4. All abundance posteriors shift significantly compared to when the radius and surface gravity are allowed to vary, though the direction of this shift varies for different species. The radial velocity and v sin i posteriors change slightly as well, though the former does not exhibit the same trimodal behavior as when the radius alone is fixed. While these constraints seem more plausible than those obtained when only the radius was fixed to a certain value, the fit to the data does suffer compared to when the radius and gravity are allowed to vary, as shown in Figure 19. Furthermore, our choice of fixed radius and surface gravity, while guided by previous studies of this object, are still relatively arbitrarily chosen. As the benefit of a retrieval analysis is to obtain constraints with fewer a priori assumptions than fitting the data to grid models, we do not use this fixed radius and gravity retrieval as our "preferred" FIRE retrieval in Section 4 for comparing to the SpeX and grid model results.

3.8. Cloudy Retrieval

In Section 3.1 we fixed our cloud parameters to be consistent with an optically thin cloud that would not affect the emission spectrum when it appeared our model was perhaps too flexible. After incorporating the preceding changes that we found improved our results (fixing β, changing the wavelength limits to match B11, sampling one data point per resolution element,

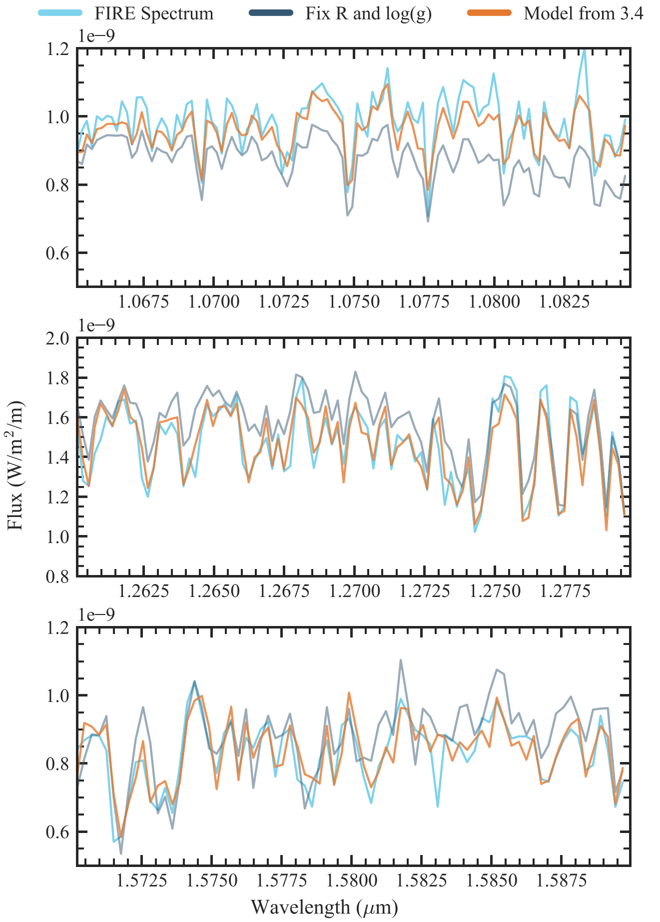

Figure 19. Select regions of the model spectrum from the median retrieved parameters when the radius and log(g) are fixed to 1 $R_{\rm Jup}$ and 4.5, respectively, compared to the median model when both are allowed to vary (from Section 3.4) and the FIRE spectrum of U0722. The fit to the data is worse when the radius and gravity are not allowed to vary in the retrieval.

updating the CH_4 and NH_3 opacities, and ignoring regions victim to poor order stitching), we allowed the cloud parameters to vary once again. Figure 20 shows the resulting TP profiles and posteriors in gray. The cloud parameters are unconstrained, except for a potential upper limit on the cloud volume mixing ratio. Other parameters are relatively unaffected, suggesting the inclusion of cloud opacity has little impact. This lack of evidence for optically thick clouds in the atmosphere of U0722 is consistent with expectations for late T dwarfs (e.g., Kirkpatrick 2005) as well as other T dwarf retrieval studies at lower spectral resolution (e.g., Line et al. 2017; Zalesky et al. 2022).

4. Discussion

4.1. SpeX versus FIRE

We choose the FIRE retrieval from Section 3.4, with pieces of the spectrum affected by order stitching removed and all the preceding changes, as our "preferred" FIRE retrieval. While Sections 3.5–3.8 explore various other tests we performed, the retrieval from Section 3.4 uses the entire wavelength range while providing more physical constraints than those gained when using the new alkali opacities or fixing the radius for example. Table 3 lists each change to our retrieval framework we tested, the section of the paper where it is discussed, and whether or not it was applied for our preferred retrieval. Figure 21 shows the FIRE spectrum compared to the median model spectrum from the initial retrieval described in Section 3.1 and the median model spectrum from this final preferred FIRE retrieval. Red lines at the top of each panel indicate data points removed from our analysis due to spurious flux values and high telluric absorption (Section 3.1) or suspected problems with order stitching (Section 3.4). In Figure 21, the model from our final retrieval fits the FIRE spectrum much better than for our initial retrieval, particularly the peak of the y band and the CH_4 features in the H band, as discussed in Section 3.3. However, though the posteriors of the retrieved parameters are quite different, there are large sections of the spectrum where both models reproduce the observed spectrum relatively well, as should be expected for a data-driven model-fitting method. Most of the tests of our framework outlined in Section 3, other than updating the line lists, were motivated by intuition or unphysical results rather than poor fits to the data. As such, we do not plot the median models from all our different retrieval runs in the interest of brevity and clarity.

Figure 22 shows how much the constraints on our retrieved posteriors improve when using the $R \sim 6000$ FIRE spectrum compared to the $R \sim 100$ SpeX spectrum. The "preferred" SpeX retrieval here uses the same updated line lists as described in Section 3.3. The H_2O, CH_4, and NH_3 abundance posteriors with FIRE are ~3–6× more precise than those from SpeX. Similarly, we can constrain the surface gravity to within about 0.04 dex, about 5× more precise than with SpeX. Furthermore, between ~0.5 to 20 bars, the TP profile is constrained within 100 K compared to the much wider 500 K spread for SpeX. Finally, our retrieval on the medium-resolution FIRE spectrum allows constraints on parameters such as H_2S abundance, CO abundance, radial velocity, and $v \sin i$ which are not constrained with the SpeX spectrum. However, while the preferred FIRE retrieval yields very precise constraints, they may not be accurate descriptions of the characteristics of U0722 and the uncertainties do not include any systematic effects, which we will discuss further below.

Table 4 lists the physical parameters of U0722 for both retrievals, as well as from previous studies which will be discussed below. To calculate a number of these quantities and their uncertainties from the parameters in our retrieval framework, we take 5000 random samples of our posterior. With these precise constraints on the molecular abundances, we can consider the metallicity and C/O ratio as most of the metal content in a cool brown dwarf atmosphere is contained in H_2O and CH_4, with some contribution from CO and NH_3. We calculate these quantities from our retrieved abundances following Equations (1) and (2) from Zalesky et al. (2022) and assuming solar abundances from Lodders (2010). To account for condensation processes that can deplete atmospheric oxygen, we multiply our H_2O abundance by 1.3 to approximate the intrinsic metallicity and C/O better, as in Zalesky et al. (2022). Our retrieved abundances yield $[M/H] = -0.10^{+0.02}_{-0.02}$ dex and $C/O = 0.54^{+0.01}_{-0.02}$ from the FIRE retrieval, with ~3–4× the precision than from the SpeX retrieval. For comparison, Zalesky et al. (2022) on average constrain [M/H] and C/O to within 0.2 dex with 50 T dwarf spectra at $R \sim 100$, although the precision varies among the objects. Though we have achieved precise constraints on these bulk properties, Calamari et al. (2022) carried out a retrieval

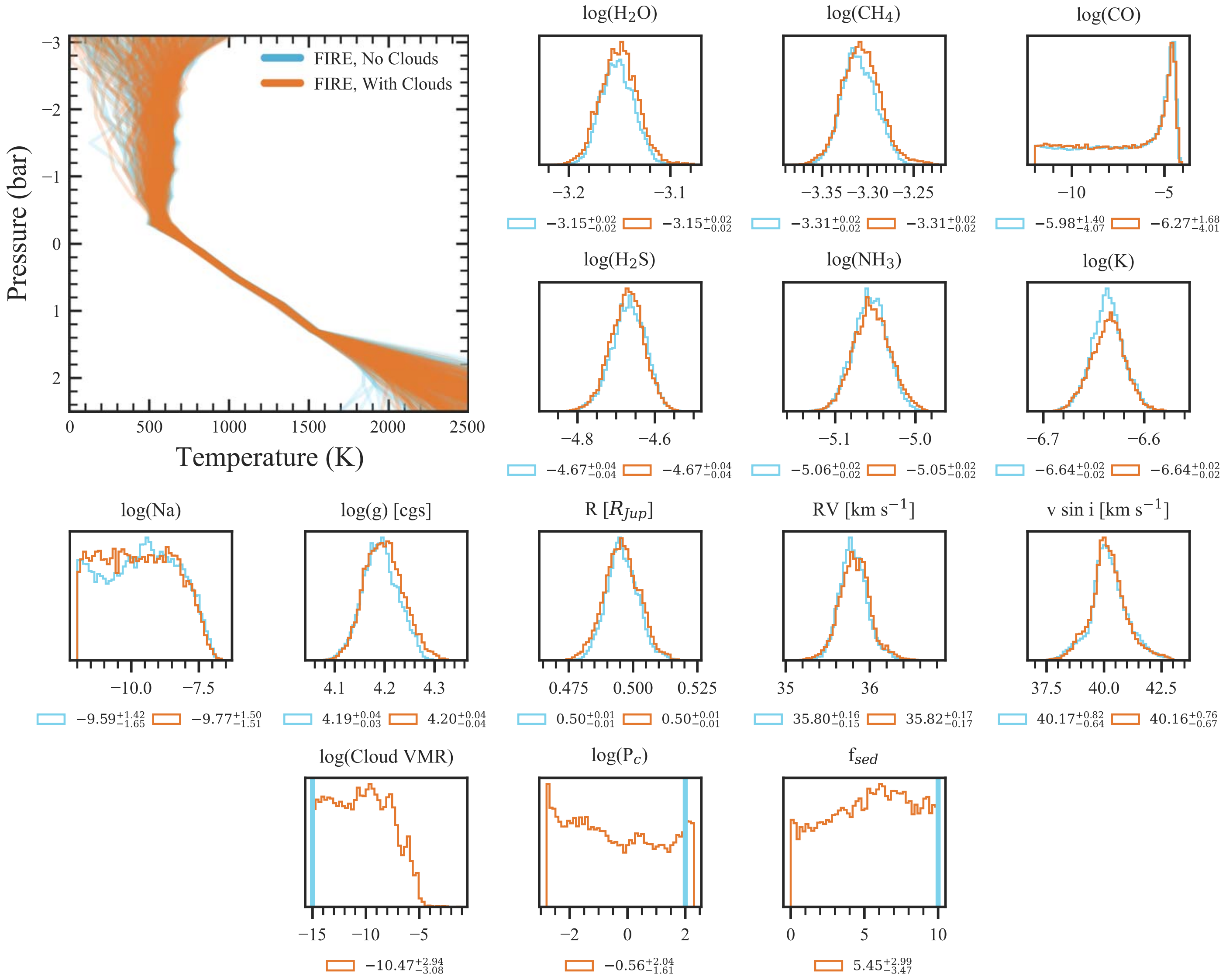

Figure 20. Effect on the retrieved TP profiles and selected posteriors of allowing the cloud parameters to vary (orange), instead of being fixed to values corresponding to optically thin clouds (blue). We find little evidence for optically thick clouds in the atmosphere of U0722.

Table 3
Changes to Our Retrieval Framework Tested for Application to the FIRE Spectrum of U0722

Change	Section of Paper	In preferred retrieval?
Add radial velocity and v sin i	2.2	yes
Mask regions of total telluric absorption	3.1	yes
Remove second TP smoothing hyperparameter	3.1	yes
Fix cloud parameters to optically thin values	3.1	yes
Limit data to 0.9–2.35 μm	3.2	yes
Take every fourth data point to not oversample the FIRE resolution element	3.2	yes
Update the NH$_3$ and CH$_4$ opacities	3.3	yes
Mask data points affected by issues with order stitching	3.4	yes
Limit analysis to subsections of the spectrum, *J*–*K*, and *H*–*K*	3.5	no
Update alkali opacities	3.6	no
Fix radius to 1 $R_{\rm Jup}$	3.7	no
Fix log(g) = 4.5 and R = 1 $R_{\rm Jup}$	3.7	no
Allow the cloud parameters to vary	3.8	no

study of GI 229B and showed the 1.3 oxygen scaling factor leads to a calculated C/O that was unexpectedly inconsistent with measurements of the primary star. They suggest that better understanding of the potential oxygen sinks in brown dwarf interiors could refine the best way to connect measured atmospheric C/O to the bulk value.

For each sample of our posterior, we also generate a low-resolution spectrum over 0.3 to 250 μm, which we integrate

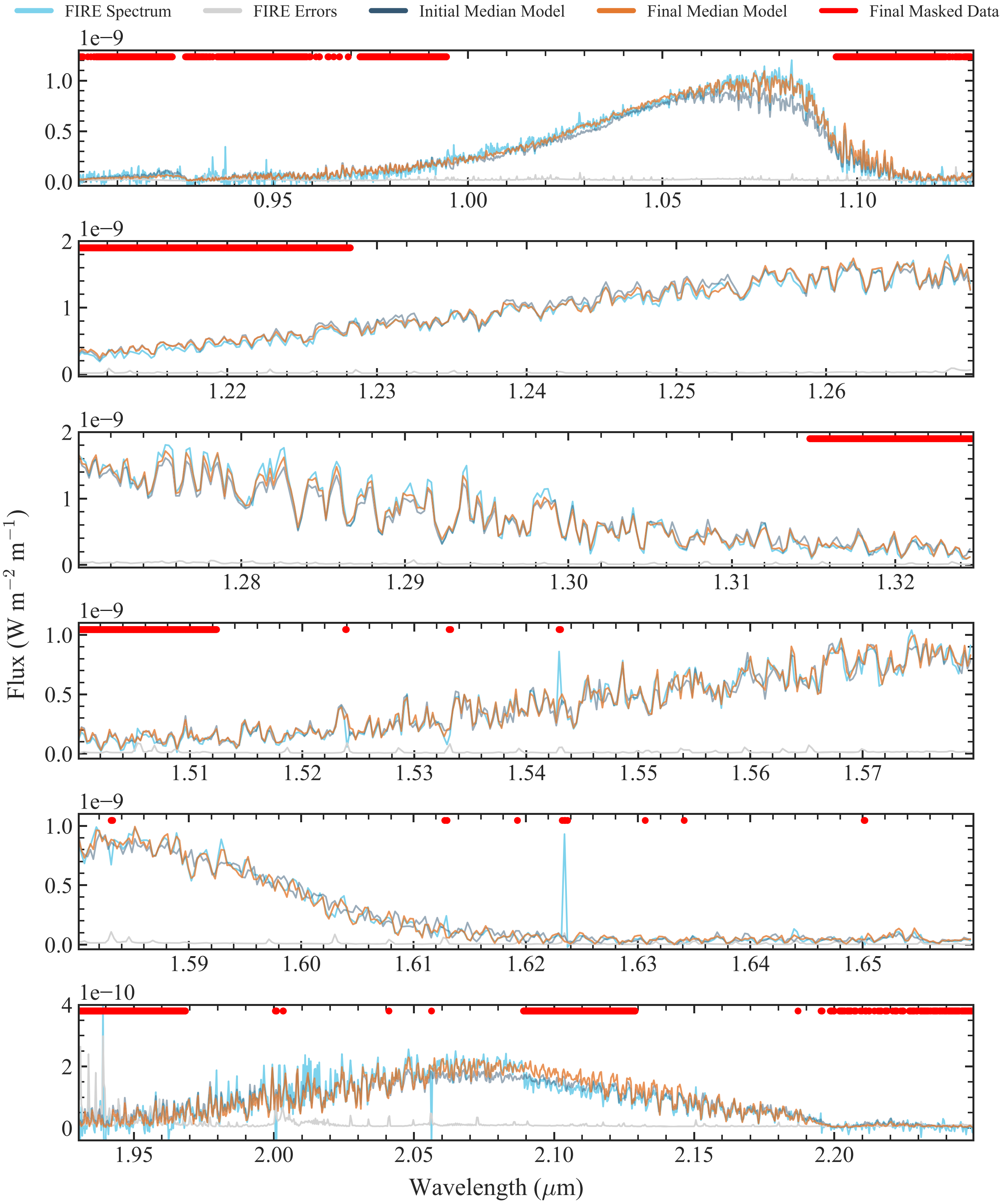

Figure 21. Comparison of the FIRE spectrum (light blue) with the median model of our initial retrieval (navy) and the median model of our "final" preferred FIRE retrieval from Section 3.4 (orange). The FIRE errors are shown in gray. Red lines at the top of each panel indicate sections of the FIRE spectrum that were removed from our final analysis as described in Sections 3.1, 3.2, and 3.4. Our final preferred median model spectrum does a better job fitting the FIRE data, particularly the peak of the y band and the CH_4 features in the H band.

and use to compute the bolometric luminosity L_{Bol} and effective temperature T_{eff}. Leggett et al. (2012) report a luminosity range of $\log(L_{Bol}/L_{Sun}) = -6.05$ to -6.17 from observed spectra of U0722 over ∼0.7–4 μm. The calculated $\log(L_{Bol}/L_{Sun})$ from the FIRE results of $-6.23^{+0.20}_{-0.09}$ is consistent with this literature value, but the luminosity from our SpeX results $\log(L_{Bol}/L_{Sun}) = -6.42^{+0.08}_{-0.05}$ is significantly lower. We also note that the luminosity constraints from the

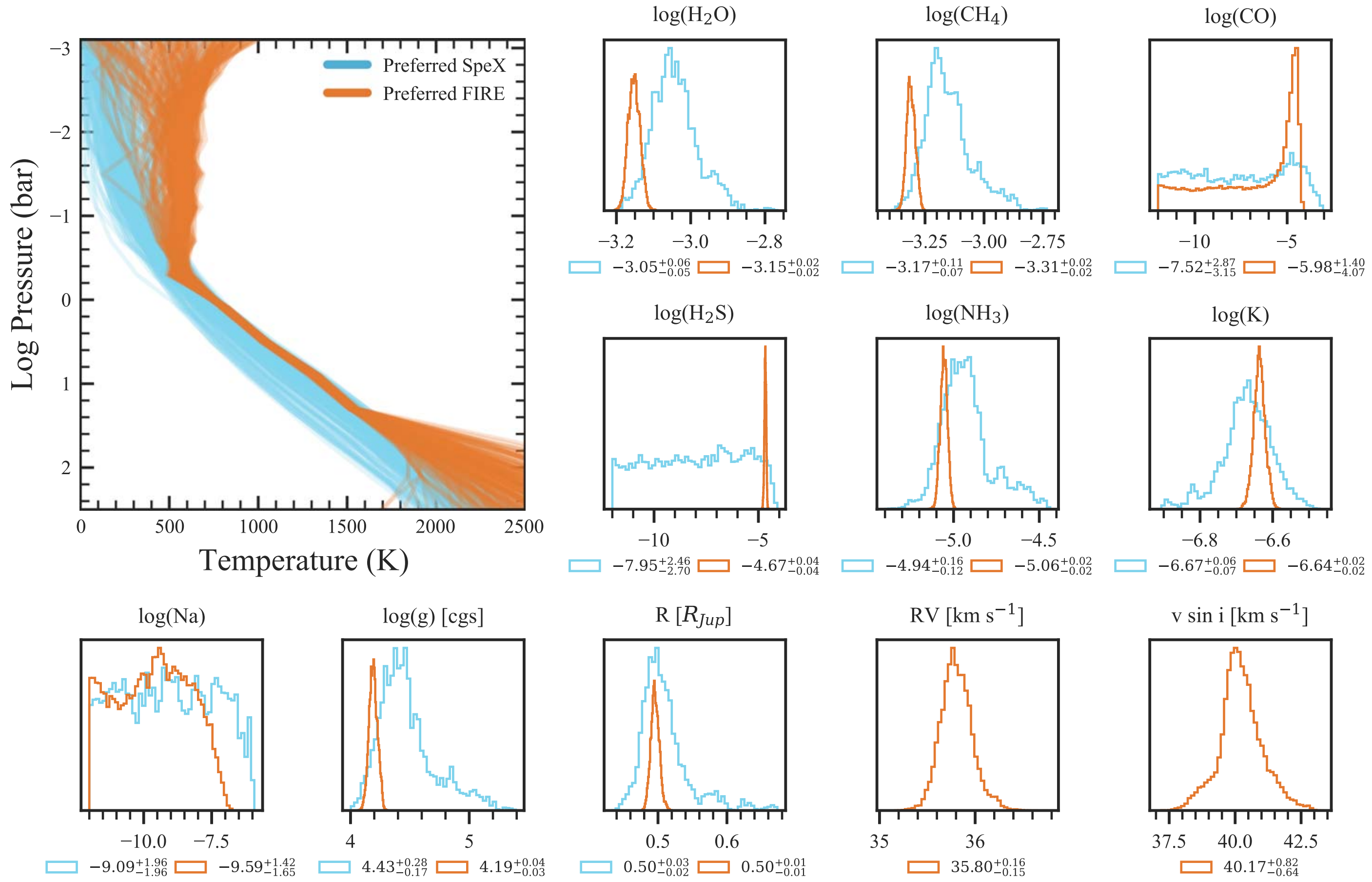

Figure 22. Retrieved TP profiles and selected posterior distributions for selected parameters of the SpeX and FIRE spectra of U0722 after making the changes discussed in Section 3.

SpeX retrieval are more precise than those from the FIRE retrieval. While between 0.5–20 bars the TP profile is much better constrained by the FIRE retrieval, outside of this range the temperatures vary considerably and are hotter than the corresponding SpeX values, leading to a calculated luminosity that is both higher and less well constrained. The effective temperatures calculated from the luminosities and radius values unsurprisingly show the same behavior.

However, both our SpeX and FIRE retrievals do result in an unphysically small radius of about 0.5 $R_{\rm Jup}$, potentially calling the accuracy of our other constraints into question. The parameter actually constrained by CHIMERA is the radius-to-distance scaling factor $(R/D)^2$; however, U0722 has a well-constrained distance from parallax measurements (4.12 ± 0.04 pc; Leggett et al. 2012) that is most likely not the source of our impossibly small radius. From the Sonora Bobcat evolutionary tracks (Marley et al. 2021), the minimum possible radius for even a 10 Gyr object at subsolar metallicity is 0.75 $R_{\rm Jup}$. Furthermore, this small radius combined with our median retrieved v sin i would imply an unreasonably fast rotation period of about 1.55 hr. Figures 7 and 9 show this radius problem particularly gets worse when updating the CH_4 and NH_3 cross sections, which are necessary to reproduce the line positions seen in the FIRE spectrum accurately. One potential source of error could be the completeness of the Hargreaves et al. (2020) CH_4 line list in the y band as discussed in Section 3.5. Furthermore, even with the previously used Yurchenko & Tennyson (2014) line list we were retrieving a smaller radius than expected (0.76 $R_{\rm Jup}$), indicating additional issues that are perhaps only exacerbated by the change to the newer CH_4 line list.

Further work is needed to assess whether our small radius could be attributed to completeness issues with the CH_4 line list from Hargreaves et al. (2020), uncertainties on how to treat alkali opacities, poor photometric calibration, or some other unseen flaw in our modeling framework. Recently, multiple retrieval studies have found radii smaller than expected from evolutionary models for both L dwarfs (Gonzales et al. 2020; Burningham et al. 2021; Xuan et al. 2022) and T dwarfs (Kitzmann et al. 2020; Lueber et al. 2022) across different retrieval frameworks and instruments with varying spectral resolutions. Furthermore, Zhang et al. (2021) performed a uniform comparison of 55 late T dwarf spectra with the Sonora Bobcat grid (Marley et al. 2021) of forward models using the Bayesian framework Starfish, finding small radii for a number of the studied objects, indicating this issue is not solely found in retrieval analyses. Notably, Zhang et al. (2021) fit a SpeX spectrum of U0722, getting $T_{eff} = 680 \pm 26$ K, $\log(g) = 3.6 \pm 0.3$ dex, $[M/H] = -0.06 \pm 0.2$ dex, and $R = 0.43 \pm 0.04$ $R_{\rm Jup}$, yielding even more unphysical values of the surface gravity and radius than in this work. More retrieval studies for large samples of brown dwarf spectra, particularly including mid-infrared data for the coolest objects and high-quality observations from JWST, will hopefully illuminate the source of this small radius problem. In addition, the growing sample of transiting brown dwarfs from the TESS mission (e.g., Šubjak

Table 4
Parameters of U0722 Calculated from This Work and Previous Studies

Parameter	FIRE Retrieval (This work)	SpeX Retrieval (This work)	BT-Settl Model Grid Fit B11	Tuned ATMO Model Grid Fit Leggett et al. (2021)
Wavelength Range (μm)	0.9–2.35	0.9–2.35	0.9–2.35	0.6–5.1
Spectral Resolution	6000	100	6000	180–500[f]
log(g) (cgs)	$4.19^{+0.04}_{-0.03}$	$4.43^{+0.28}_{-0.17}$	$4.0^{+0.3}_{-0.3}$	4.5
Radius ($R_{\rm Jup}$)	$0.5^{+0.01}_{-0.01}$	$0.5^{+0.03}_{-0.02}$	$1.14^{+0.46}_{-0.33}$[a]	1.12[g]
Distance (pc)	Fixed at 4.12	Fixed at 4.12	4.6 (restricted)[b] 49 (unrestricted)	Fixed at 4.12
Mass ($M_{\rm Jup}$)	$1.5^{+0.1}_{-0.1}$	$1.9^{1.2}_{-0.6}$	5.24[c]	15[g]
C/O	$0.54^{+0.01}_{-0.02}$	$0.55^{+0.08}_{-0.06}$	0.55[d]	0.55[h]
[M/H] (dex)	$-0.10^{+0.02}_{-0.02}$	$-0.02^{+0.07}_{-0.06}$	0.0[d]	0.0[h]
log(L_{Bol}/L_{Sun})	$-6.23^{+0.20}_{-0.09}$	$-6.42^{+0.08}_{-0.05}$	−6.11 (restricted)[e] −5.52 (unrestricted)	−5.99[e]
T_{eff} (K)	711^{+84}_{-35}	638^{+32}_{-15}	500^{+50}_{-50} (restricted) 700^{+50}_{-50} (unrestricted)	540

Notes.

[a] Calculated from the reported log(g) and mass.

[b] B11 perform two fits, one with distance as a free parameter and one where the model-derived distance must be within 5σ of the parallax measurement from Lucas et al. (2010).

[c] Determined from the evolutionary models of Baraffe et al. (2003) and the best-fit T_{eff} and log(g).

[d] Considered models from the BT-Settl model grid (Allard & Freytag 2010) assuming solar metallicity and C/O using the solar abundances from Asplund et al. (2009).

[e] Calculated from radius and T_{eff}.

[f] Used flux-calibrated spectral energy distribution with data sets from multiple instruments published by Lucas et al. (2010), Leggett et al. (2012), and Miles et al. (2020).

[g] Determined from the evolutionary models of Phillips et al. (2020).

[h] Considered models from the ATMO grid (Phillips et al. 2020) assuming solar C/O and with [M/H] = −0.5, 0.0, and +0.3 dex using the solar abundances reported by Asplund et al. (2009) and updated by Caffau et al. (2011).

et al. 2020; Carmichael et al. 2022) can provide independent tests of the radii predicted by evolutionary models, though their irradiated nature may cause difficulty in making comparisons.

4.2. Comparison to the Results of B11

We can compare the results from our preferred retrieval on the FIRE spectrum of U0722 to the original analysis of the data set presented by B11. By comparing the spectrum to line lists, they were able to identify features of H_2O, CH_4, and NH_3, as well as broad absorption from K. Similarly, we are able to place constraints on the abundances of all of these species to within ±0.02 dex, indicating the impact of these species on the spectrum even if the retrieved abundances are not exactly accurate. In addition, we are also able to constrain the H_2S abundance due to a few distinct H_2S features in the spectrum (see Section 3.3.2) unidentified in the previous study.

B11 fit the FIRE spectrum of U0722 with BT-Settl models of Allard et al. (2011) based on the fitting procedure outlined by Cushing et al. (2008). The large differences we see in the retrieved posteriors when looking at subsections of the spectrum in Section 3.5 reflect similar variance across the model fits of B11 of the data in the different bandpasses. However, the authors find significant differences between the best-fitting models and the data in many places across the spectrum. Furthermore, there are notable discrepancies in our retrieved physical values from those of B11 when considering their full spectrum fit (most analogous to our results) as shown in Table 4. While their log(g) $= 4.0^{+0.3}_{-0.3}$ is consistent, they report a larger mass of 5.24 $M_{\rm Jup}$ from evolutionary models, indicating a much larger radius value of $1.14^{+0.46}_{-0.33}$ $R_{\rm Jup}$. Due to the large uncertainty on U0722's parallax at the time, B11 allow the distance instead of the radius to vary when fitting the $(R/d)^2$ scaling factor. When allowing this distance to vary freely, their best fit to the entire spectrum also prefers a hotter object with an effective temperature of 700 ± 50 K, consistent with the calculated T_{eff} from our FIRE retrieval but with a far larger distance than the literature value (49 pc versus 4.12 pc). Our retrieval functionally achieves the same effect with a small $(R/d)^2$ scaling factor instead attributed to a small radius given the reliable parallax measurement. However, when the distance is required to be within 5σ of the parallax measurement from Lucas et al. (2010), the authors get a much colder T_{eff} of 500 ± 50 K.

Finally, while their measured v sin i of 40 ± 10 km s^{-1} agrees with our results, their radial velocity measurement of 46.9 ± 2.5 km s^{-1} is significantly higher than our result of 35.80 ± 0.15 km s^{-1}. Given that the radial velocity was measured in part with models using significantly older line lists for basically all molecules present in this object's spectrum, such an inconsistency is perhaps expected. Future work to calculate if an updated radial velocity measurement would change the original determination by B11 of a thin disk Galactic orbit could provide interesting context to U0722's potential age and evolutionary trajectory, though the change in radial velocity may not be enough to matter. We use the tool Bayesian Analysis for Nearby Young AssociatioNs Σ (BANYANΣ; Gagné et al. 2018) to determine the probability of U722 being a member of any well-characterized young associations within 150 pc, inputting the previously measured proper motion (Faherty et al. 2009) and parallax (Faherty et al. 2012) as well as the radial velocity measured in this work. BANYANΣ gives a 99.9% likelihood that U0722 is a field

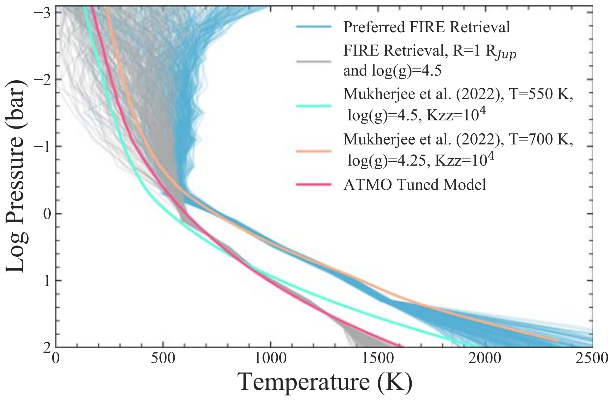

Figure 23. TP profiles from our preferred FIRE retrieval (blue) and the fixed radius and surface gravity retrieval (gray) to the tuned ATMO model (pink) and two disequilibrium forward models from Mukherjee et al. (2022). The tuned ATMO model is significantly colder than the retrieved TP profiles from our preferred FIRE retrieval, and has a different gradient in accordance with the adjusted adiabat discussed by Leggett et al. (2021). However, the retrieved TP profiles when fixing the radius and surface gravity to set values is in excellent agreement with the tuned ATMO model.

brown dwarf. Furthermore, for both velocity parameters our reported precision from `emcee` is significantly higher than those reported for the measurements by B11. Both the radial velocity and $v \sin i$ were calculated by cross-correlating the 1.27–1.31 μm section of FIRE spectrum with a template, either a grid model spectrum or another observation of a T dwarf, which may or may not be a good fit to the data in question. In contrast, the log-likelihood-based MCMC approach reported here both considers significantly more data points across the whole spectrum and has been shown to produce smaller error bars than cross-correlation methods (Brogi & Line 2019).

4.3. Comparison to Grid Models

Given the many advances in line lists over the past decade, it is instructive to look at more recent comparisons of U0722 spectra with grid models. Miles et al. (2020) find that the low-resolution ($R \sim 300$) M-band spectrum of U0722 indicates disequilibrium amounts of CO from vertical mixing, consistent with our tentative detection of CO in the FIRE spectrum. Leggett et al. (2021) compare a flux-calibrated 0.6–5.1 μm spectrum of U0722 created from multiple published observations (Lucas et al. 2010; Leggett et al. 2012; Miles et al. 2020) with the ATMO 2020 grid of models, finding that the models with and without disequilibrium chemistry still have trouble fitting the data well. The authors improve this fit by “tuning” the gradient of the TP profile away from the standard adiabat. As such, we compare our retrieved results to this adiabat-adjusted model in Table 4, which has an effective temperature of 540 K, log surface gravity (cgs) of 4.5, solar metallicity, log Kzz ($\mathrm{cm}^2\ \mathrm{s}^{-1}$) = 7, and an adiabatic index of 1.27.

Figure 23 shows our retrieved TP profiles from the FIRE spectrum of U0722, compared to the abundances of the tuned ATMO model (P. Tremblin 2021, private communication), as well as two forward grid models with disequilibrium chemistry from Mukherjee et al. (2022). The tuned ATMO TP profile has a steeper gradient than either of the other grid models, reflecting the adjusted adiabat. Our retrieved TP profiles from the preferred FIRE retrieval are significantly hotter than that of the tuned ATMO model, more closely resembling that of a hotter 700 K object from the Mukherjee et al. (2022) grid, consistent with our calculated T_{eff}. The difference in temperature is consistent with the differences in radii; the tuned ATMO model assumed a radius of 1.12 R_{Jup} from the evolutionary models of Phillips et al. (2020), more than double that of our retrieved value. Thus, a cooler object would be necessary to achieve a similar amount of flux. In fact, when we fixed the radius to 1 R_{Jup} and surface gravity to $\log(g) = 4.5$, as discussed in Section 3.7, the retrieved TP profiles are consistent with the tuned ATMO model as shown by the gray curves in Figure 23. This agreement is reasonable, as Leggett et al. (2021) similarly set R and log(g) to values from an evolutionary model before tuning the TP profile to match the observed data.

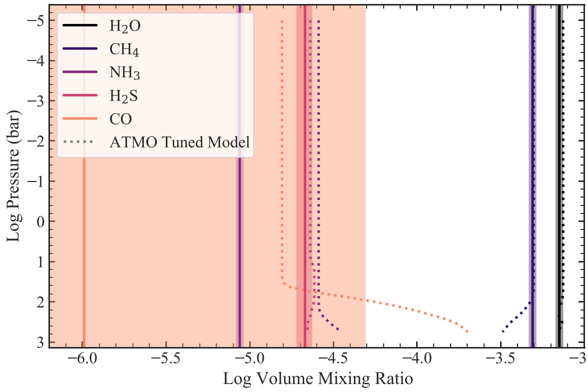

Figure 24. Molecular volume mixing ratios from the tuned ATMO model (dotted lines) as a function of atmospheric pressure compared to the median and 1σ posteriors from our FIRE retrieval (solid lines and shaded regions). With the exception of NH_3, the abundances are quite similar.

Figure 24 compares our retrieved molecular abundances, shown by the solid lines and shaded 1σ regions, to the mixing ratios in the tuned ATMO model as a function of pressure in the atmosphere. Unlike the tuned ATMO model, which assumes disequilibrium chemistry governed by the eddy diffusion parameter $\log(K_{zz})$, our volume mixing ratios for each species are allowed to vary independently and are not tied to one another by any assumptions or parameterizations of the chemical timescales involved. Our retrieved values for CO, CH_4, and H_2S are all in agreement with the ATMO abundances above 100 bars, and our H_2O value posterior is only 0.003 dex away from the ATMO model value. However, our NH_3 posterior is $\sim$0.5 dex lower, perhaps reflecting the differences in effective temperature and surface gravity between our retrieval results and the tuned ATMO model. Given a measured CO abundance, we can estimate $\log(K_{zz})$ by comparing to chemical equilibrium abundances from the Sonora Bobcat structure models (Marley et al. 2021) of similar T_{eff} and log(g) as described by Miles et al. (2020). Since our CO abundance has large uncertainties, our results could imply no vertical mixing for the lowest amount of CO up to $\log(K_{zz}) \sim 3.3\ \mathrm{cm}^2\ \mathrm{s}^{-1}$ for the maximum amount of CO. The comparatively larger $\log(K_{zz}) = 7\ \mathrm{cm}^2\ \mathrm{s}^{-1}$ from the tuned ATMO model is needed to get a similar CO abundance for a much colder object with a higher surface gravity. While our retrieved surface gravity and radius are unphysical, our molecular abundances are plausible and mostly consistent with grid model predictions. The similarity in molecular abundances is also reflected in the consistency of the C/O ratios and metallicities reported in Table 4.

Differences in the data considered perhaps help explain why our retrieval prefers a hotter, smaller object than the tuned

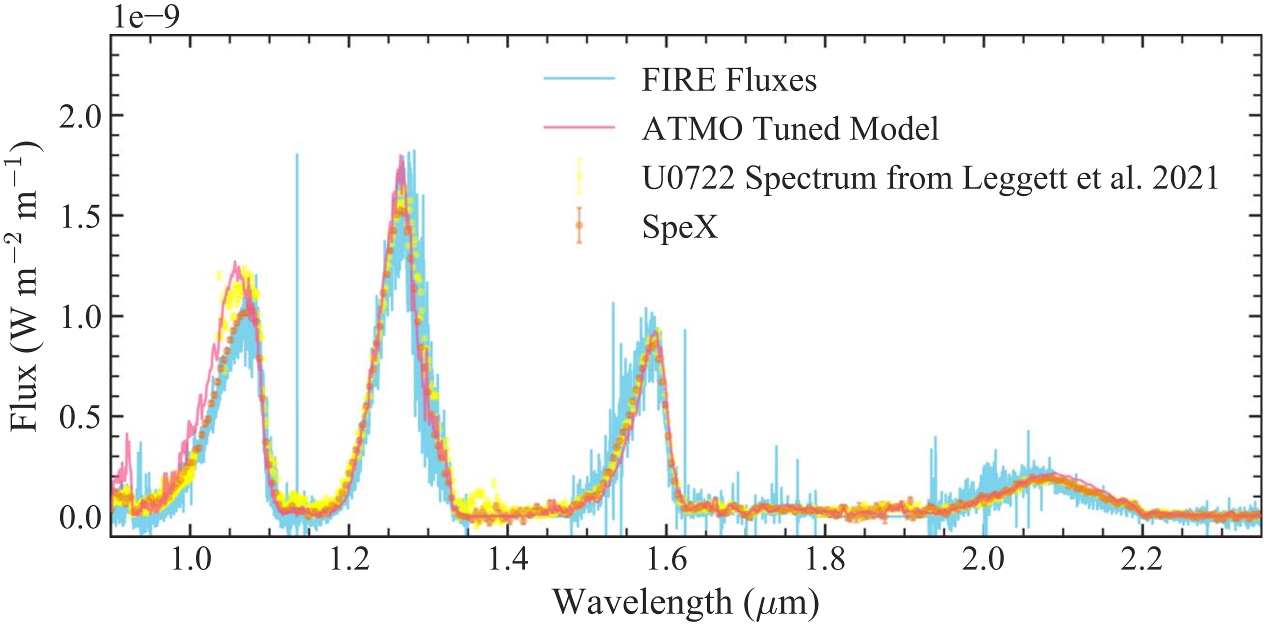

Figure 25. Comparison of the FIRE (blue) and SpeX (orange) spectra of U0722 analyzed in this work to the spectrum (yellow) and tuned ATMO model (pink) used in Leggett et al. (2021). There are notable discrepancies in the peak of the y band.

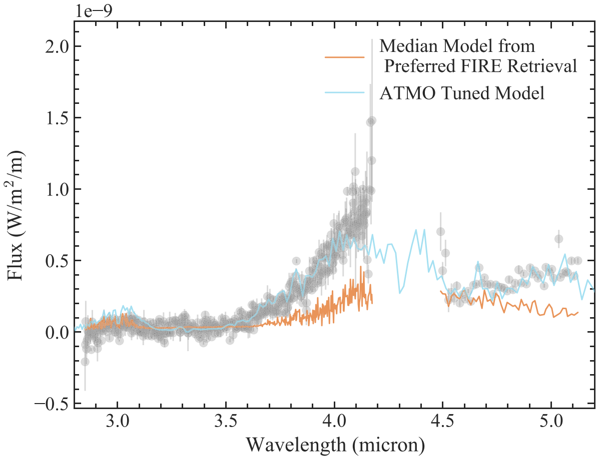

Figure 26. Comparison of the median model of our preferred FIRE retrieval and the ATMO tuned model to the L- and M-band spectra included in the analysis of Leggett et al. (2021). The FIRE retrieval clearly does not reproduce the measured flux of U0722 at longer wavelengths, whereas the ATMO tuned model gets closer at matching the observed slopes of these regions of the spectrum.

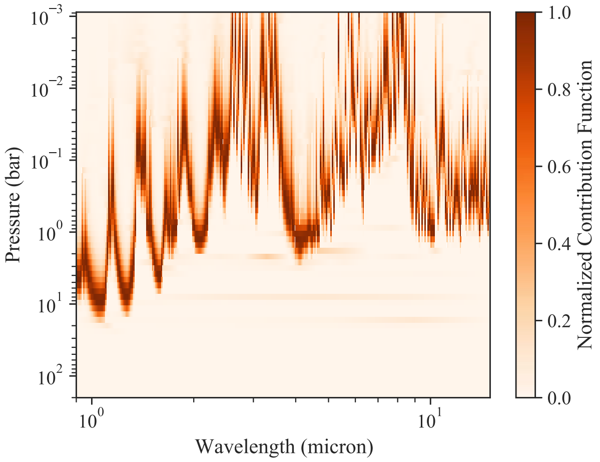

Figure 27. Normalized contribution functions for a model generated from the median results of preferred FIRE retrieval (which covered 0.9–2.5 μm) extrapolated out to longer wavelengths.

ATMO model when the retrieval is solely driven by the data (rather than any assumed radius or gravity value). We note that the near-infrared portion of the U0722 spectrum used in Leggett et al. (2021) is slightly inconsistent with that of the FIRE and SpeX spectra examined in this work. Figure 25 shows all three data sets, as well as the tuned ATMO model; the peak y-band flux in the Leggett et al. (2021) spectrum is offset in both strength and wavelength. While the source of this discrepancy is unclear, it undoubtedly contributes to differences in our fitted or retrieved values for U0722. However, a more important distinction is the inclusion of longer-wavelength data for U0722 in the analysis of Leggett et al. (2021).

The authors included L- and M-band spectra from Leggett et al. (2012) and Miles et al. (2020), respectively. Figure 26 shows these data sets compared to the median model from our preferred FIRE retrieval extrapolated out to these wavelengths, as well as the tuned ATMO model. Our model clearly underpredicts the observed flux of U0722 and does not reproduce the observed slope in the M-band data. Figure 27 shows the normalized contribution functions for a model using the median parameter values from our preferred FIRE retrieval, generated at lower resolution and out to ∼15 μm. The L and M bands probe the upper atmosphere, and we note that if we were to perform a retrieval on these data sets we would need to extend the atmosphere in our radiative transfer model to pressures below 10^{-3} bars, the current top of the atmosphere in this framework. Notably, the TP profile from our preferred FIRE retrieval is not well constrained at these low pressures in our retrieval, perhaps contributing to the model's failure to reproduce these data points. Furthermore, the discrepancy in the M band could be due to less CO present in the median model than is needed to fit the data, as it is a major opacity source in this wavelength region. Figure 24 shows that the median CO abundance from our preferred FIRE retrieval is more than a dex less than the amount of CO in the tuned ATMO model. In combination with the unphysically small radius, the inability of our preferred FIRE retrieval to produce fluxes in accordance with longer-wavelength observations points to our precise constraints on the atmosphere of U0722 being inaccurate and not necessarily representative of the true physical properties of this object. Future work on combining medium-resolution spectra with broader wavelength coverage data at lower resolution may provide further insight into the best way to obtain more plausible results from an atmospheric retrieval analysis.

5. Conclusions

In this work, we have applied the CHIMERA atmospheric retrieval framework to a high signal-to-noise, medium-resolution ($R \sim 6000$) FIRE spectrum of a T9 dwarf. Key takeaways from this work are as follows:

1. *Limitations of the data set must be taken into account.* In Section 3.2, we show that ensuring only one data point per resolution element is sampled as well as cutting out very noisy regions of data at either end of the spectrum can affect our retrieved posteriors. More dramatically, areas of the spectrum where orders were stitched poorly can negatively bias the retrieval analysis as discussed in Section 3.4. Future improvements to order-stitching methods, or new ways to account for potential stitching issues within a retrieval framework, could help alleviate this problem in future analysis of data from echelle spectrographs.
2. *Using different opacity sources may lead to very different results.* Updating the line lists for CH_4 and NH_3 to those from Hargreaves et al. (2020) and Coles et al. (2019), respectively, greatly improved the ability of the forward models to match the line positions in the data, as shown in Figure 8. Almost all retrieved posteriors were affected by this change, even for the retrieval on the $R \sim 100$ SpeX spectrum as shown in Figures 7 and 9. For example for the FIRE retrieval, changing the line lists lead the median abundances of H_2O and CH_4 to increase by ~0.3 dex and the surface gravity $\log(g)$ to increase by ~0.4 dex. However, the updated line lists also resulted in a radius decreased by about 30% to an unphysical 0.5 R_{Jup}. We also tested different treatments of the Na and K opacities in Section 3.6, again finding largely disparate results depending on which cross sections were used. While we do recommend the Hargreaves et al. (2020) CH_4 line list due to its ability to match the line positions in our FIRE spectrum, more comparison with other line lists with regards to completeness as well as treatment of the alkali wings are needed to utilize fully this kind of high-quality data.
3. *Medium-resolution retrievals offer very precise constraints, but they may not be accurate.* As shown in Figure 22, the constraints on the TP profile and abundances from our FIRE retrieval of U0722 are significantly more precise than those from the SpeX spectrum. In particular, we are able to retrieve the abundances of H_2S and tentatively CO, which is not possible with the lower-resolution spectrum. However, while we do get these precise, stellar-like constraints on atmospheric abundances (~0.02 dex), the radius is far too small to be physically plausible. This small size is in accordance with our retrieved TP profile being hotter than previous analyses of this object, yielding a similar overall observed flux. Thus, this study joins a growing number of modeling analyses of brown dwarf spectra that have yielded smaller radii than allowed by our understanding of brown dwarf evolution. Furthermore, extrapolating a median model from our retrieval to the L and M bands cannot reproduce the observations of U0722 at these wavelengths, indicating the constraints from the medium-resolution FIRE spectrum alone do not accurately describe the conditions of this object.

This work is a first foray into the challenges and benefits of applying atmospheric retrieval tools to medium-resolution spectra of brown dwarfs. With the launch of JWST and future ground-based studies, more work is needed to assess how we can improve our current modeling frameworks to address these challenges and unlock the potential for trustworthy, precise constraints on substellar atmospheres from retrievals of medium-resolution spectra.

Acknowledgments

We thank the anonymous reviewer for their thoughtful comments and suggestions that have improved the quality of this work. We acknowledge use of the lux supercomputer at UC Santa Cruz, funded by NSF MRI grant AST 1828315. This work benefited from the 2022 Exoplanet Summer Program in the Other Worlds Laboratory (OWL) at the University of California, Santa Cruz, a program funded by the Heising-Simons Foundation. M.R.L. acknowledges support from NASA XRP grant 80NSSC19K0293. J.J.F. acknowledges support from NSF Award No. 1909776 and NASA Award No. 80NSSC22K0142 as well as the Simons Foundation.

Appendix

To further illustrate the correlations among the parameters in our preferred FIRE retrieval, a corner plot summarizing the posteriors of selected parameters is shown in Figure 28.

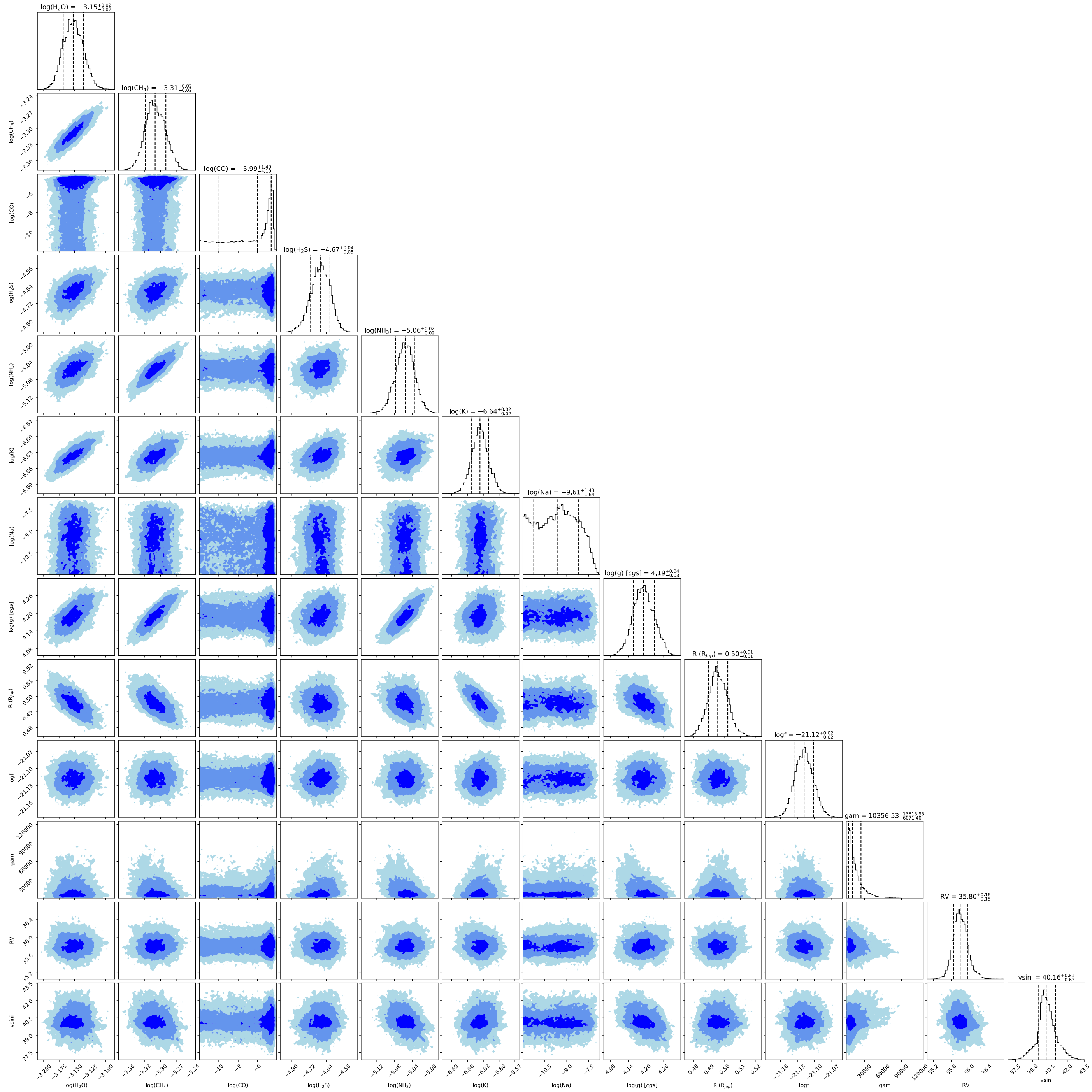

Figure 28. Corner plot summarizing the posteriors of our preferred FIRE retrieval for the listed parameters. Correlations between parameters are shown in the two-dimensional histograms. Marginalized posteriors for each parameter are shown along the diagonal, with the dashed lines indicating the 16th, 50th, and 84th percentiles. The median and $\pm 1\sigma$ values for each parameter are shown above the histograms.

ORCID iDs

Callie E. Hood https://orcid.org/0000-0003-1150-7889
Jonathan J. Fortney https://orcid.org/0000-0002-9843-4354
Michael R. Line https://orcid.org/0000-0002-2338-476X
Jacqueline K. Faherty https://orcid.org/0000-0001-6251-0573

References

Ackerman, A. S., & Marley, M. S. 2001, ApJ, 556, 872
Allard, F., Allard, N. F., Homeier, D., et al. 2007a, A&A, 474, L21
Allard, F., & Freytag, B. 2010, HiA, 15, 756
Allard, F., Homeier, D., & Freytag, B. 2011, in ASP Conf. Ser. 448, 16th Cambridge Workshop on Cool Stars, Stellar Systems, and the Sun, ed. C. Johns-Krull, M. K. Browning, & A. A. West (San Francisco, CA: ASP), 91
Allard, N. F., Kielkopf, J. F., & Allard, F. 2007b, EPJD, 44, 507
Allard, N. F., Spiegelman, F., & Kielkopf, J. F. 2016, A&A, 589, A21
Allard, N. F., Spiegelman, F., Leininger, T., & Molliere, P. 2019, A&A, 628, A120
Asplund, M., Grevesse, N., Sauval, A. J., & Scott, P. 2009, ARA&A, 47, 481
Azzam, A. A. A., Lodi, L., Yurchenko, S. N., & Tennyson, J. 2015, JQSRT, 161, 41

Baraffe, I., Chabrier, G., Barman, T. S., Allard, F., & Hauschildt, P. H. 2003, A&A, 402, 701
Benneke, B., & Seager, S. 2012, ApJ, 753, 100
Bochanski, J. J., Burgasser, A. J., Simcoe, R. A., & West, A. A. 2011, AJ, 142, 169
Brogi, M., & Line, M. R. 2019, AJ, 157, 114
Burgasser, A. J. 2014, ASI Conf. Ser. 11, International Workshop on Stellar Spectral Libraries, ed. H. P. Singh, P. Prugniel, & I. Vauglin, 7
Burningham, B., Faherty, J. K., Gonzales, E. C., et al. 2021, MNRAS, 506, 1944
Burningham, B., Marley, M. S., Line, M. R., et al. 2017, MNRAS, 470, 1177
Burrows, A., Hubbard, W. B., Lunine, J. I., & Liebert, J. 2001, RvMP, 73, 719
Burrows, A., & Volobuyev, M. 2003, ApJ, 583, 985
Caffau, E., Ludwig, H. G., Steffen, M., Freytag, B., & Bonifacio, P. 2011, SoPh, 268, 255
Calamari, E., Faherty, J. K., Burningham, B., et al. 2022, ApJ, 940, 164
Canty, J. I., Lucas, P. W., Yurchenko, S. N., et al. 2015, MNRAS, 450, 454
Carmichael, T. W., Irwin, J. M., Murgas, F., et al. 2022, MNRAS, 514, 4944
Coles, P. A., Yurchenko, S. N., & Tennyson, J. 2019, MNRAS, 490, 4638
Cushing, M. C., Kirkpatrick, J. D., Gelino, C. R., et al. 2011, ApJ, 743, 50
Cushing, M. C., Marley, M. S., Saumon, D., et al. 2008, ApJ, 678, 1372
Czesla, S., Schröter, S., Schneider, C. P., et al. 2019, PyA: Python astronomy-related packages, Astrophysics Source Code Library, ascl:1906.010
Faherty, J. K., Burgasser, A. J., Cruz, K. L., et al. 2009, AJ, 137, 1
Faherty, J. K., Burgasser, A. J., Walter, F. M., et al. 2012, ApJ, 752, 56
Faherty, J. K., Riedel, A. R., Cruz, K. L., et al. 2016, ApJS, 225, 10
Fletcher, L. N., Irwin, P. G. J., Teanby, N. A., et al. 2007, Icar, 189, 457
Foreman-Mackey, D., Hogg, D. W., Lang, D., & Goodman, J. 2013, PASP, 125, 306
Freedman, R. S., Lustig-Yaeger, J., Fortney, J. J., et al. 2014, ApJS, 214, 25
Freedman, R. S., Marley, M. S., & Lodders, K. 2008, ApJS, 174, 504
Gagné, J., Mamajek, E. E., Malo, L., et al. 2018, ApJ, 856, 23
Gonzales, E. C., Burningham, B., Faherty, J. K., et al. 2020, ApJ, 905, 46
Gonzales, E. C., Burningham, B., Faherty, J. K., et al. 2021, ApJ, 923, 19
Gonzales, E. C., Burningham, B., Faherty, J. K., et al. 2022, ApJ, 938, 56
Gordon, I. E., Rothman, L. S., Hill, C., et al. 2017, JQSRT, 203, 3
Gray, D. F. 2008, The Observation and Analysis of Stellar Photospheres (Cambridge: Cambridge Univ. Press)
Hargreaves, R. J., Gordon, I. E., Rey, M., et al. 2020, ApJS, 247, 55
Hoch, K. K. W., Konopacky, Q. M., Barman, T. S., et al. 2022, AJ, 164, 155
Howe, A. R., McElwain, M. W., & Mandell, A. M. 2022, ApJ, 935, 107
Kirkpatrick, J. D. 2005, ARA&A, 43, 195
Kitzmann, D., Heng, K., Oreshenko, M., et al. 2020, ApJ, 890, 174
Leggett, S. K., Saumon, D., Marley, M. S., et al. 2012, ApJ, 748, 74
Leggett, S. K., Tremblin, P., Phillips, M. W., et al. 2021, ApJ, 918, 11
Li, G., Gordon, I. E., Rothman, L. S., et al. 2015, ApJS, 216, 15
Line, M. R., Fortney, J. J., Marley, M. S., & Sorahana, S. 2014, ApJ, 793, 33
Line, M. R., Marley, M. S., Liu, M. C., et al. 2017, ApJ, 848, 83
Line, M. R., Teske, J., Burningham, B., Fortney, J. J., & Marley, M. S. 2015, ApJ, 807, 183
Line, M. R., Wolf, A. S., Zhang, X., et al. 2013, ApJ, 775, 137
Lodders, K. 2010, in Formation and Evolution of Exoplanets, ed. R. Barnes (New York: Wiley), 157
Lucas, P. W., Tinney, C. G., Burningham, B., et al. 2010, MNRAS, 408, L56
Lueber, A., Kitzmann, D., Bowler, B. P., Burgasser, A. J., & Heng, K. 2022, ApJ, 930, 136
Lupu, R. E., Zahnle, K., Marley, M. S., et al. 2014, ApJ, 784, 27
Madhusudhan, N., & Seager, S. 2009, ApJ, 707, 24
Marley, M. S., & Robinson, T. D. 2015, ARA&A, 53, 279
Marley, M. S., Saumon, D., Visscher, C., et al. 2021, ApJ, 920, 85
Miles, B. E., Skemer, A. J. I., Morley, C. V., et al. 2020, AJ, 160, 63
Mukherjee, S., Fortney, J. J., Batalha, N. E., et al. 2022, ApJ, 938, 107
Petrus, S., Chauvin, G., Bonnefoy, M., et al. 2023, A&A, 670, L9
Phillips, M. W., Tremblin, P., Baraffe, I., et al. 2020, A&A, 637, A38
Piette, A. A. A., & Madhusudhan, N. 2020, MNRAS, 497, 5136
Polyansky, O. L., Kyuberis, A. A., Zobov, N. F., et al. 2018, MNRAS, 480, 2597
Rey, M., Nikitin, A. V., & Tyuterev, V. G. 2017, ApJ, 847, 105
Richard, C., Gordon, I. E., Rothman, L. S., et al. 2012, JQSRT, 113, 1276
Rodgers, C. D. 2000, Inverse Methods for Atmospheric Sounding: Theory and Practice (Singapore: World Scientific)
Rothman, L. S., Gordon, I. E., Babikov, Y., et al. 2013, JQSRT, 130, 4
Rothman, L. S., Gordon, I. E., Barber, R. J., et al. 2010, JQSRT, 111, 2139
Simcoe, R. A., Burgasser, A. J., Schechter, P. L., et al. 2013, PASP, 125, 270
Tannock, M. E., Metchev, S., Hood, C. E., et al. 2022, MNRAS, 514, 3160
Tennyson, J., & Yurchenko, S. N. 2012, MNRAS, 425, 21
Toon, O. B., McKay, C. P., Ackerman, T. P., & Santhanam, K. 1989, JGR, 94, 16287
Šubjak, J., Sharma, R., Carmichael, T. W., et al. 2020, AJ, 159, 151
Wakeford, H. R., & Sing, D. K. 2015, A&A, 573, A122
Wang, J., Kolecki, J. R., Ruffio, J.-B., et al. 2022, AJ, 163, 189
Xuan, J. W., Wang, J., Ruffio, J.-B., et al. 2022, ApJ, 937, 54
Yurchenko, S. N., Barber, R. J., & Tennyson, J. 2011, MNRAS, 413, 1828
Yurchenko, S. N., & Tennyson, J. 2014, MNRAS, 440, 1649
Zalesky, J. A., Line, M. R., Schneider, A. C., & Patience, J. 2019, ApJ, 877, 24
Zalesky, J. A., Saboi, K., Line, M. R., et al. 2022, ApJ, 936, 44
Zhang, Z., Liu, M. C., Marley, M. S., Line, M. R., & Best, W. M. J. 2021, ApJ, 921, 95